Wide band gap kesterite absorbers for thin film solar cells: potential and challenges for their deployment in tandem devices

Bart Vermang, Guy Brammertz, Marc Meuris, Thomas Schnabel, Erik Ahlswede, Leo Choubrac, Sylvie Harel, Christophe Cardinaud, Ludovic Arzel, Nicolas Barreau, et al.

▶ **To cite this version:**

Bart Vermang, Guy Brammertz, Marc Meuris, Thomas Schnabel, Erik Ahlswede, et al.. Wide band gap kesterite absorbers for thin film solar cells: potential and challenges for their deployment in tandem devices. Sustainable Energy & Fuels, 2019, 3 (9), pp.2246-2259. 10.1039/c9se00266a . hal-02291073

HAL Id: hal-02291073
https://hal.science/hal-02291073

Submitted on 5 Apr 2024

HAL is a multi-disciplinary open access archive for the deposit and dissemination of scientific research documents, whether they are published or not. The documents may come from teaching and research institutions in France or abroad, or from public or private research centers.

L'archive ouverte pluridisciplinaire **HAL**, est destinée au dépôt et à la diffusion de documents scientifiques de niveau recherche, publiés ou non, émanant des établissements d'enseignement et de recherche français ou étrangers, des laboratoires publics ou privés.

WIDE BAND GAP KESTERITE ABSORBERS FOR THIN FILM SOLAR CELLS: POTENTIAL AND CHALLENGES FOR THEIR DEPLOYMENT IN TANDEM DEVICES

Bart Vermang[1,2,3], Guy Brammertz[1,2,3], Marc Meuris[1,2,3], Thomas Schnabel[4], Erik Ahlswede[4], Leo Choubrac[5], Sylvie Harel[5], Christophe Cardinaud[5], Ludovic Arzel[5], Nicolas Barreau[5], Joop van Deelen[6], Pieter-Jan Bolt[6], Patrice Bras[7], Yi Ren[7], Eric Jaremalm[7], Samira Khelifi[8,9], Sheng Yang[8], Johan Lauwaert[8], Maria Batuk[10], Joke Hadermann[10], Xeniya Kozina[11], Evelyn Handick[11], Claudia Hartmann[11], Dominic Gerlach[12], Asahiko Matsuda[13], Shigenori Ueda[14,15], Toyohiro Chikyow[12,13], Roberto Félix[11], Yufeng Zhang[11,16], Regan G. Wilks[11,17], and Marcus Bär[11,17,18,19]

[1]imec division IMOMEC – partner in Solliance, Wetenschapspark 1, 3590 Diepenbeek, Belgium

[2]Hasselt University – partner in Solliance, Martelarenlaan 42, 3500 Hasselt, Belgium

[3]EnergyVille, Thorpark 8320, 3600 Genk, Belgium

[4]ZSW, Meitnerstrasse 1, 70563 Stuttgart, Germany

[5]Institut des Matériaux Jean Rouxel (IMN), Université de Nantes, CNRS, 2 rue de la Houssinière, 44322 Nantes, France

[6]TNO – partner in Solliance, High Tech Campus 21, 5656 AE Eindhoven, The Netherlands

[7]Midsummer AB, Elektronikhöjden 6, 175 43 Järfälla, Sweden

[8]Department of Electronics and Information Systems (ELIS), Ghent University, Technologiepark Zwijnaarde 15, 9052 Gent, Belgium

[9]Department of Solid State Sciences, Ghent University, Krijgslaan 281-S1, 9000 Gent, Belgium

[10]Electron Microscopy for Materials Science (EMAT), University of Antwerp, Groenenborgerlaan 171, 2020 Antwerp, Belgium

[11]Department Interface Design, Helmholtz-Zentrum Berlin für Materialien und Energie GmbH (HZB), Hahn-Meitner-Platz 1, 14109 Berlin, Germany

[12]International Center for Materials Nanoarchitectonics (MANA), National Institute for Materials Science (NIMS), 1-1 Namiki, Tsukuba, Ibaraki 305-0044, Japan

[13]Research and Services Division of Materials Data and Integrated System (MaDIS), National Institute for Materials Science (NIMS), 1-1 Namiki, Tsukuba, Ibaraki 305-0044, Japan

[14]Synchrotron X-ray Station at SPring-8, National Institute for Materials Science (NIMS), 1-1-1 Kouto, Sayo-cho, Hyogo 679-5148, Japan

[15]Research Center for Advanced Measurement and Characterization, National Institute for Materials Science (NIMS), 1-2-1, Sengen, Tsukuba, Ibaraki 305-0047, Japan

[16]College of Physical Science and Technology, Xiamen University (XMU), 361005, Xiamen, China

[17]Energy Materials In-Situ Laboratory Berlin (EMIL), Helmholtz-Zentrum Berlin für Materialien und Energie GmbH (HZB), Albert-Einstein-Str. 15, 12489, Berlin, Germany

[18]Department of Chemistry and Pharmacy, Friedrich-Alexander-Universität Erlangen-Nürnberg, 91058 Erlangen, Germany

[19]Helmholtz-Institute Erlangen-Nürnberg for Renewable Energy (HI ERN), 12489 Berlin, Germany

CORRESPONDING AUTHOR – Bart Vermang, Martelarenlaan 42, 3500 Hasselt, Belgium

BROADER CONTEXT

The power conversion efficiency of the dominant single junction photovoltaic technology is approaching its theoretical limit. Further progress, with higher efficiencies and lower cost, requires improving current technologies in new ways, whilst using cheap, abundant materials. An approach to increase the efficiency is the construction of double junction solar cells combining a top and bottom cell in a tandem device. If an established technology – such as crystalline silicon – is used for the bottom cell, a relatively wide band gap material is needed for the top cell. An ideal top cell would be low-cost and be made of abundant, non-toxic materials. Typical top cell candidates that have been presented have some significant drawbacks: Perovskite top cells, for example, contain toxic elements and have well-known stability issues. III-V top cells are well studied for concentrators, but are too costly for tandem applications. In this contribution, we report on our detailed fundamental analysis of a new candidate absorber material, namely high band gap kesterite films. The Sn in the standard $Cu_2ZnSn(S,Se)_4$ kesterite structure is replaced by Ge (or Si), increasing the band gap to a level where it is of interest in tandem configurations. This study describes the potential and the challenges that are involved with the use of wide band gap kesterite absorbers in future tandem devices.

ABSTRACT

This work reports on developments in the field of wide band gap Cu_2ZnXY_4 (with X = Sn, Si or Ge, and Y = S, Se) kesterite thin film solar cells. An overview on recent developments and the current understanding of wide band gap kesterite absorber layers, alternative buffer layers, and suitable transparent back contacts is presented. $Cu_2ZnGe(S,Se)_4$ absorbers with absorber band gaps up to 1.7 eV have been successfully developed and integrated into solar cells. Combining a CdS buffer layer prepared by an optimized chemical bath deposition process with a 1.36 eV band gap absorber resulted in a record $Cu_2ZnGeSe_4$ cell efficiency of 7.6 %, while the highest open-circuit voltage of 730 mV could be obtained for a 1.54 eV band gap absorber and a Zn(O,S) buffer layer. Employing $InZnO_x$ or TiO_2 protective top layers on SnO_2:In transparent back contacts yields 85-90 % of the solar cell performance of reference cells (with Mo back contact). These advances show the potential as well as the challenges of wide band gap kesterites for future applications in high-efficiency and low-cost tandem photovoltaic devices.

KEYWORDS

Thin-film solar cells, wide band gap, kesterite, germanium, semi-transparent

1. INTRODUCTION

World-record single-junction solar cell efficiencies of monocrystalline silicon-wafer (Si) and thin-film (TF) solar cells are 26.7 % and 22.9 % [1,2], respectively, thus approaching their theoretical (Shockley-Queisser) limit of 30 % under standard illumination conditions [3]. One approach to increase the efficiency of solar cells above this limit is the construction of tandem devices. A tandem device consists of two solar cells: a wide band gap (E_G) solar cell (in which the photovoltaically active absorber material has an optical band gap of 1.5-2.0 eV) harvests the high-energy photons and a small band gap solar cell (in which the absorber has a band gap of 1.0-1.5 eV) harvests the low-energy photons. This approach can lead to theoretical efficiencies of up to 44 % under 1-sun illumination [4].

With a band gap of 1.1 eV [4], Si-wafer-based devices are the ideal bottom cell candidate, but many prominent top cell candidates have issues related to abundancy, toxicity, stability, or cost [5]. Therefore, we consider kesterite-based devices as potential top cells for tandem device applications, because $Cu_2ZnSn(S,Se)_4$-type kesterite solar cells are stable, made out of abundant and non-toxic components, and already achieve relatively high performance [1]. Depending on the [S]/([S]+[Se]) composition, the band gap of the kesterite absorber can be tuned between 1.0 and 1.5 eV [6]. Highest efficiencies for $Cu_2ZnSn(S,Se)_4$-based devices are achieved when absorbers with band gaps between 1.1 and 1.2 eV are employed [7], which is too low for efficient (top) tandem solar cell applications. However, (partially) replacing tin atoms with silicon or germanium atoms has the potential to result in kesterite absorbers with band gaps even above 1.5 eV [8,9]. This work aims to give an overview on the recent development and current understanding of (i) these wide band gap kesterite absorber layers, (ii) alternative (non-toxic) buffer layer candidate materials, and (iii) suitable transparent back contacts (TBCs) allowing tandem configuration. A summary of recently published results is complemented with new experimental findings and a theoretical study of the efficiency potential of devices based on wide band gap kesterite absorbers. Thus, the paper aims at covering all aspects of deploying kesterite wide-band gap absorbers as top cells in tandem solar cell applications in order to identify inherent bottlenecks that may limit device performance and present generally valid optimization approaches and first results to lay the foundation and pave the way for future more detailed studies that undeniably have to follow.

2. EXPERIMENTAL, RESULTS, AND DISCUSSION

2.1. ABSORBER LAYER

First, we give an overview of the absorber layer formation, in which two main approaches are applied, i.e. sequential evaporation (Section 2.1.1) and solution-based deposition (Section

2.1.2). The first approach (respective samples are henceforth called → EVAP-*sample*) is more convenient to study different metal components and is, therefore, used to investigate the replacement of Sn atoms with Si or Ge in EVAP-$Cu_2ZnSn(S,Se)_4$ absorber layers; while in the second approach (→ SOL-*sample*), the focus is on the replacement of Sn with Ge and the optimization of the involved wet chemistry. Note that there will inherently be variations in properties of the kesterite absorbers deposited by the different methods (i.e., using sequential evaporation or solution-based deposition), however the findings that are presented in the manuscript – while not exactly transferrable – mainly relate to universally relevant conditions that will arise in cell production regardless of the absorber deposition method.

2.1.1. EVAPORATION-BASED PROCESS

The polycrystalline absorber layers are fabricated using a two-step vacuum-based approach; see Figure S1. Soda lime glass (SLG) substrates of 1.3 mm thickness are used, on which a 150-nm-thick Si(O,N) diffusion barrier is first deposited, followed by a 400-nm-thick Mo layer. The thin Si(O,N) diffusion barrier is deposited in order to avoid the diffusion of elements from the glass substrate into the absorber. Early tests have shown that the evaporated absorber quality is better if this diffusion barrier is added. On top of this substrate, a multilayer of different metals is deposited using a Pfeiffer PLS 500 evaporation system. For accurate layer thickness control, a quartz microcrystal balance is used. This metal multilayer is then annealed in an Annealsys As-One 150 rapid thermal annealing system that is equipped with a 10 % H_2Se (diluted in N_2) gas line and a 100 % H_2S gas line. This way, the layers are selenized or sulfurized under a continuous flow of H_2Se or H_2S. During this selenization/sulfurization step, a polycrystalline layer is formed with typical grain sizes in the order of 0.5 to 1 µm.

2.1.1.1. Si-BASED COMPOUNDS

We have used metal layer stacks, including Si, to explore the possibility of fabricating EVAP-$Cu_2ZnSiSe_4$, -$Cu_2Zn(Si,Sn)Se_4$, -Cu_2SiSe_3, -Cu_2SiS_3, -Cu_8SiSe_6, and -Cu_8SiS_6 layers [10]. Unfortunately, the Si appears to be largely unreactive at processing temperatures below 600 °C, which is the maximum temperature allowed for SLG substrates. Only EVAP-Cu_8SiSe_6 and EVAP-Cu_8SiS_6 could be produced in a reliable way, without significant presence of secondary phases, leading to polycrystalline absorber layers with high-intensity photoluminescence (PL) peaks at energies of 1.35 (for EVAP-Cu_8SiSe_6) and 1.84 eV (EVAP-Cu_8SiS_6) [11]. However, no functioning solar cells could be fabricated with these absorber layers, as the doping seemed to be too high (in the order of 10^{18} cm^{-3} or higher), and the minority carrier lifetime seemed to be lower than 0.2 ns, leading to functioning diodes but no photocurrent. One observation that could also explain the absence of any photoactivity is the formation of SiO_2 during absorber processing. Figure 1 shows hard x-ray photoelectron spectroscopy (HAXPES) survey spectra of an EVAP-Cu_8SiS_6 sample before (black) and after (red) sulfurization treatment. Upon sulfurization, the O and Na (most likely diffused from the

SLG substrate) contents increase. The inset shows the region of the Si 2s and S 2p core level lines compared to reference positions of silicon compounds [12]. The Si 2s line of the sulfurized layer stack shifts to higher binding energies compared to the Si 2s peak before sulfurization. The comparison with the reference positions indicates the conversion of Si-Si into $Si-S_2$ and/or $Si-O_2$ bonds. The fact that the S 2p line can only be clearly observed on a magnified (x 25) scale together with the high O 1s intensity for the sample after sulfurization, however, suggests that the surface region of the sulfurized sample has mainly a SiO_2 character, which would prevent efficient charge carrier transport.

2.1.1.2. Ge-BASED COMPOUNDS

For the fabrication of polycrystalline EVAP-$Cu_2ZnGeSe_4$ layers, we have used 180 nm of Ge, 125 nm of Zn and 170 nm of Cu as starting layers [13]. These layer thicknesses were chosen in order to end up with a Zn-rich and Cu-poor composition of the absorber layer, with Cu/(Zn+Ge) = 0.9 and Zn/Ge = 1.05. This metal stack was then selenized for 15 minutes in a continuous flow of H_2Se at a temperature of 460 °C. The resulting absorber layer is polycrystalline with a typical grain size in the order of 500 nm. Figure S2 shows a cross-section scanning electron microscopy (SEM) image of a finished solar cell stack, exemplifying the grain morphology of the absorber as well as the other layers of the solar cell stack. A Bragg Brentano X-ray diffraction (XRD) measurement of a finished absorber layer on a Mo back contact clearly shows the $Cu_2ZnGeSe_4$ peaks with a small contribution of a ZnSe secondary phase, as a small shoulder of the main $Cu_2ZnGeSe_4$ peaks at angles around 27.3 and 45.3 degrees, shown in Figure 2. Due to the Zn-rich nature of the absorber layer, the presence of ZnSe secondary phase has to be expected. $Cu_{2-x}Se$ and $GeSe_2$ secondary phases cannot be identified within the accuracy of the XRD measurements. Also note that the peaks of the ternary phase Cu_2GeSe_3 overlap with the main peaks of the $Cu_2ZnGeSe_4$ phase completely, making it impossible to distinguish these phases by XRD. To visualize the secondary phases, cross-section energy dispersive X-ray spectroscopy (EDX) elemental maps of the absorber were acquired in scanning transmission electron microscopy (STEM) mode, shown in Figure 3. The observed regions of elemental inhomogeneities are attributed to ZnSe – which seems to be present in large amounts at the top surface of the absorber – and Cu_2GeSe_3 / $Cu_{2-x}Se$ phases – which are present more at the grain boundaries and at the backside Mo interface. Some of the absorbers were lift-off in order to record Raman spectra near the EVAP-$Cu_2ZnGeSe_4$/Mo interface. Both sides (front absorber and at the back side, i.e. near the back contact) were analyzed. At the front $Cu_2ZnGeSe_4$ side (as published in [29]), only $Cu_2ZnGeSe_4$ is clearly detected, but presence of Cu_2GeSe_3 and $Cu_{2-x}Se$ cannot be excluded as their Raman peaks overlap with $Cu_2ZnGeSe_4$. At the back side only 2H-$MoSe_2$ related peaks are observed. Time and energy resolved photoluminescence measurements (not shown) reveal a PL peak at an energy of about 1.36 eV, with a decay time in the order of 2 ns. The band gap of this

absorber is thus too small to be employed as a top cell of tandem devices. However, due to the high throughput of the evaporation process route/equipment, a large number of respective EVAP-$Cu_2ZnGeSe_4$ samples are available and were thus (for practical reasons and to allow for good statistics) chosen for most of our optimization efforts with respect to the absorber surface treatment (see Section 2.2.1), the buffer layer (see Section 2.2.2), and the TBC (see Section 2.4).

2.1.2. Ge-BASED COMPOUNDS BY SOLUTION-BASED PROCESS

The SOL-$Cu_2ZnGe(S,Se)_4$ absorbers were deposited in a two-step process as schematically drawn in Figure S3. A metal salt solution was deposited onto a Mo-coated SLG substrate by doctor-blade coating with subsequent drying on a hot plate. Different solvents, metal salts and chalcogen sources have been evaluated in a previous manuscript [14]. Here, the chemical composition of the absorbers is Cu/(Zn+Ge)=0.7 and Zn/Ge=1.0 which is slightly more Cu-poor than the EVAP-$Cu_2ZnGeSe_4$ layers. The chemical and electronic structure of respective SOL-$Cu_2ZnGe(S,Se)_4$ absorbers and, in particular, the impact of the absorber formation by annealing in Se-atmosphere has been monitored by lab-based soft x-ray photoelectron spectroscopy (XPS) and synchrotron-based HAXPES. The XPS measurements were performed in the off-synchrotron analysis chamber at EMIL in ultra-high vacuum (base pressure < 5×10^{-10} mbar) employing a non-monochromatized Mg K_α (1253.56 eV) x-ray tube (PREVAC RS40B1) as excitation source. The photoelectrons were detected by a Scienta Omicron Argus CU electron analyzer. HAXPES was measured at beamline BL15XU at SPring-8 using an excitation energy of 6 keV and a Scienta R4000 electron analyzer (see [15,16] for more details on the experimental setup; same measurement conditions apply for the data shown in Figure 1). Figure 4 shows the XPS S 2p/Se 3p (left panel) and HAXPES shallow core level (right panel) spectra of a SOL-$Cu_2ZnGe(S,Se)_4$ sample prepared from a solution of Cu-, Zn- and Ge-oxides in water and ammonium thioglycolate. Upon selenization, a clear Se 3d signal in the shallow core level region and the Se 3p core level dominating the S 2p/Se 3p energy region can be observed. The fit of the spectrum with S 2p and Se 3p doublets (see top spectrum in Figure 4 – left panel) reveals the presence of at least two Se species, and two S species – where the secondary (S) peak most likely indicates the presence of S-O_x and Se-O_x (with $x \geq 3$). The presence of Se-O_x is also indicated by the high-binding energy shoulder of the Se 3d line in the shallow core level region (and depicted in the right panel of Figure 4). Quantifying the fit results yields a (surface) [S]/([S]+[Se])-ratio of approximately 0.1, significantly lower than the bulk composition of 0.3 [14]. The chemical environment of S in the absorber precursor layer (i.e., before selenization) is also rather complex – as indicated by the broad S 2p spectrum with a low binding energy shoulder (in the bottom spectrum in Figure 4 – left panel), which significantly deviates from the expected spectral shape of a S 2p doublet (see blue fit component on the top spectrum). The shallow core level photoemission

lines additionally reveal that the selenization process impacts the Zn/Cu ratio (the Cu 3p line intensity is significantly increased) and the chemical bonding environment of Ge (see inset of Figure 4 – right panel). Presumably, oxidized Ge is converted to form Ge-Se bonds upon selenization. Finally, the location of the valence band maximum at 0.2 (±0.1) eV (below the Fermi level), indicated by the arrow in Figure 4 (right panel), is in agreement with a p-type doped material, which can generally be observed for these kinds of absorbers.

To fabricate solar cells, CdS buffer layers are deposited by chemical-bath deposition (CBD) followed by a sputtered ZnO and ZnO:Al layer. Although the band alignment of $Cu_2ZnGe(S,Se)_4$ with CdS is believed to be non-ideal, in a direct comparison with potential alternative buffer layer candidate materials a CdS buffer was found to result in the highest efficiencies [17]. The morphology of a SOL-$Cu_2ZnGe(S,Se)_4$ absorber with CdS buffer can be seen in the cross-section transmission electron microscopy (TEM) image displayed in Figure S4(a). It shows two distinct layers within the SOL-$Cu_2ZnGe(S,Se)_4$: larger grains on top and smaller grains at the bottom. Note that the CdS layer on top of the absorber is only 50 nm thick and therefore hard to identify in this image. All elements are for the most part homogeneously distributed within the absorber layer; therefore, only the distribution of Zn signal is shown in Figure S4(b), where some brighter spots in the large-grain layer can be seen, which we interpret as indication for the presence of a $Zn(S,Se)_2$ secondary phase. Additionally, the signal of carbon residues that arise from thiourea is displayed in Figure S4(c). Here carbon is only present in the small-grain layer, whereas the large-grain layer is mostly carbon-free. With a higher magnification (not shown), an amorphous layer covering the $Cu_2ZnGe(S,Se)_4$ particles can be seen. The distribution of Cd [Figure S4(d)] shows that, in contrast to other investigations of kesterite absorbers with a CBD-processed CdS buffer [18], no major diffusion of Cd into the absorber layer can be detected.

Our standard solution-based deposition approach results in SOL-$Cu_2ZnGe(S,Se)_4$ absorber material with a band gap of around 1.5 eV [14]. For application in tandem solar cells, a slightly higher absorber band gap would be advantageous. One possible means to increase the band gap would be a partial or complete cation substitution, e.g., Si for Ge [9], Ag for Cu [19], or Ba for Zn [20]. However, a more complicated phase diagram is expected when using additional elements, and so we focus on increasing the band gap by tuning the anion composition (i.e., the [S]/([S]+[Se])-ratio), a well-established method for $Cu_2ZnSn(S,Se)_4$ absorbers. In general, the anion composition can be controlled (i) in the metal salt solution and/or (ii) during the annealing process. It is used in slight excess to ensure that enough S is present to form the kesterite phase during the drying step on a hot plate. If one would like to lower the band gap of the SOL-$Cu_2ZnGe(S,Se)_4$ absorber, thiourea could partly or completely be replaced by selenourea to decrease the [S]/([S]+[Se])-ratio or fabricate S-free SOL-$Cu_2ZnGeSe_4$ absorbers. However, further increasing the amount of thiourea would only

lead to excess chalcogen that cannot be incorporated into the kesterite lattice (and also more residual carbon and nitrogen) and does, therefore, not lead to an increase of the [S]/([S]+[Se])-ratio and thus absorber band gap. Therefore, we focus on increasing the [S]/([S]+[Se])-ratio during the annealing step, following approach (ii). The most obvious procedure would be to anneal the sample in the simultaneous presence of Se and S. However, the boiling point of S is 445°C [21], considerably lower than the annealing temperature of 550°C, and thereby does not allow a constant S supply during the annealing. Therefore, GeS is used as an additional sulfur source [22], which is expected to release S into the gas phase via the following reaction:

$$GeS(s) + Se(g) \leftrightharpoons GeSe(s) + S(g)$$

To allow for fine-tuning of the absorber band gap, the amount of GeS was varied between 0 and 100 mg. As a result, S is incorporated into the kesterite lattice, as can be seen from the shift of the 112-reflection in the XRD patterns displayed in Figure 5. Using Vegard's law the [S]/([S]+[Se])-ratio can be estimated based on this data, revealing that it varies in a range between 0.27 and 0.50 [22]. However, the peak shape of the 112-reflections slightly changes with the amount of GeS. Starting from 40 mg (resulting in an absorber with a band gap of 1.67 eV [22]), a shoulder at higher diffraction angles is visible, indicating the coexistence of an orthorhombic phase that is known to occur for high [S]/([S]+[Se])-ratios in $Cu_2ZnGe(S,Se)_4$ absorbers [23].

To evaluate the influence on the solar cell performance, the current density-voltage [i.e., J(V)] characteristics of the best solar cells from SOL-$Cu_2ZnGe(S,Se)_4$ absorbers with external quantum efficiency (EQE)-derived band gaps of 1.5, 1.6 and 1.7 eV (corresponding to [S]/([S]+[Se])-ratios of 0.27, 0.39, and 0.50, respectively) are compared in Figure 6; the corresponding cell parameters are listed in Table 1. As expected, the short-circuit current density (J_{SC}) decreases with increasing absorber band gap. The open circuit voltage (V_{OC}) increases considerably from 617 to 683 mV when the absorber band gap is increased from 1.5 to 1.6 eV, but decreases for the 1.7 eV absorber. The fill factor (FF) shows a slight decrease with absorber band gap, and efficiency reducing from 6.0 to 2.7 %. The loss in V_{OC} for devices based on absorbers with a band gap larger than 1.6 eV represents the most crucial loss in this sample series, which might be linked to the above-mentioned coexistence of a kesterite and an orthorhombic phase. However, the band alignment between absorber and buffer layer might also become severely performance limiting, especially for solar cells based on 1.7 eV band gap $Cu_2ZnGe(S,Se)_4$ absorbers. To make these absorbers viable for application as top cells for tandem configurations, significant efficiency enhancements are required (see discussion below). In order to achieve this improvement of wide band gap kesterite solar cell efficiencies, an optimization of all layers in the TF layer stack, especially the buffer/absorber interface, has to be performed (see Section 2.2).

2.2. SURFACE TREATMENT AND BUFFER LAYER OPTIMIZATION

For the absorber layers discussed in Section 2.1, two paths toward optimization of performance were pursued: (i) selective etching of the ZnSe secondary phases (mentioned in Section 2.1.1.2) was successfully carried out and the impact on the final solar cell properties was determined (as discussed in Section 2.2.1). (ii) The CdS buffer layer deposition was optimized, and the employment of alternative buffer layers evaluated (as discussed in Section 2.2.2). Due to its better availability this work – unless stated otherwise – was done on evaporated EVAP-$Cu_2ZnGeSe_4$ absorbers.

2.2.1. ABSORBER SURFACE TREATMENT

Various absorber characterizations techniques reveal the presence of ZnSe at the surface of EVAP-$Cu_2ZnGeSe_4$ kesterites prepared by the two-step process of evaporating metal layers in vacuum with subsequent selenization of the layer stack (detailed in Section 2.1.1.2). The presence of secondary phases at the absorber/buffer interface is usually reported to have a deleterious effect on the efficiency of the resulting solar cells [24]. To prevent this, a (selective) chemical etching process for ZnSe is included as part of the standard procedure to prepare efficient solar cells. To find the proper etching procedure, we identified two previously reported etching strategies: (i) acidic etching with hot HCl, and (ii) an oxidation route at room temperature with $KMnO_4$ in a sulfuric acid medium [25]. Raman spectroscopy with an excitation wavelength of 458 nm allows detection of even small traces of ZnSe due to the resonant measurement conditions (i.e., excitation energy is close to the band gap of ZnSe, ≈ 2.7 eV) [26], hence, (resonant) Raman spectroscopy was used as the main characterization tool to aid in determining the optimal experimental etching conditions (temperature, concentration, duration) that result in a ZnSe-free EVAP-$Cu_2ZnGeSe_4$ surface. For approach (i), this means etching with a 12 wt% HCl solution, see Figure 7. For approach (ii), a 2-minute etch at room temperature in an aqueous solution of 1 mol/L $KMnO_4$ in 1 mol/L H_2SO_4 is sufficient to effectively remove ZnSe. Ultimately, the HCl etching was chosen as the standard etching procedure based on practical arguments (parameter control, processing, and solution stability). The optimized HCl etching conditions used in standard solar cell manufacturing have been determined to be: 15 min etching in a 12 wt% HCl solution at a temperature of 80 °C.

Solar cells were prepared based on EVAP-$Cu_2ZnGeSe_4$ absorbers (from the same batch) grown on Mo coated Si(O,N)/SLG, followed by CBD of CdS buffer layer, sputtering of an i-ZnO/ZnO:Al window bi-layer and finalized by e-beam deposition of Ni/Al/Ni grids for the front contact. Two absorbers served as references (i.e., not etched) and three were HCl treated at 60, 70, and 80 °C. Resonant Raman spectra confirm that only the untreated

references contain ZnSe at the surface. The effect of this etching procedure on V_{OC}, FF, and EQE are presented in Figures 8 and 9. The V_{OC} of the cells prepared with untreated references are in the range of 500-550 mV, which corresponds to 45-50 % of the maximum achievable V_{OC} ($V_{OC,max}$) for such an absorber band gap (i.e., PL peak at 1.36 eV). In comparison, high-efficiency $Cu_2ZnSn(S,Se)_4$ solar cells typically achieve 55-60% of $V_{OC,max}$ [27]. The lower V_{OC} observed here with Ge-kesterite solar cells is suspected to partially originate from a non-ideal buffer/absorber interface (allowing for charge carrier recombination). The presence of ZnSe on the surface of the absorber (or at the buffer/absorber interface) may explain the losses. This explanation is supported by the fact that V_{OC} is significantly improved for solar cells for which the EVAP-$Cu_2ZnGeSe_4$ absorber underwent prior HCl etching (resulting in a ZnSe free absorber surface), reaching around 55 % of $V_{OC,max}$. Despite this significant V_{OC} improvement, solar cells prepared with HCl-treated absorbers result in lower efficiencies due to a dramatic FF loss and an EQE drop at longer wavelength (usually ascribed to a reduced collection length).

To determine the origin of the FF and collection length losses after HCl etching, surface characterization by HAXPES has been performed at the HiKE endstation [15] equipped with a Scienta R4000 electron analyzer and located at the BESSY II KMC-1 beamline [16] at HZB, using an excitation energy of 2.1 keV. The HAXPES survey spectra of an as-deposited (i.e., not etched; black spectrum) and a HCl etched EVAP-$Cu_2ZnGeSe_4$ sample (red spectrum) are shown in Figure 10. All $Cu_2ZnGeSe_4$-related photoemission and Auger lines can be observed, as expected. In addition, signals related to oxygen (O 1s), carbon (C 1s), and for the as-deposited EVAP-$Cu_2ZnGeSe_4$ also cadmium (Cd 3d) can be observed. The presence of oxygen and carbon can be attributed to a surface contamination layer formed due to the (short) air exposure of the samples. The significant increase of the C 1s line upon HCl etching is most likely related to additional contamination during the etching procedure. The presence of cadmium on the as-deposited sample is ascribed to cross contamination from CdS/EVAP-$Cu_2ZnGeSe_4$ samples that have been transported in the same sample box. Due to these varied and significant states of surface contamination, we deliberately refrain from attempting to quantify the HAXPES data but rather discuss them qualitatively. The HAXPES survey spectrum of the as-deposited EVAP-$Cu_2ZnGeSe_4$ sample is dominated by Zn and Se signals. Upon HCl etching, the Zn- and Se-related signals are significantly reduced, and the Cu/Zn ratio is enhanced, in good agreement with the Raman results discussed above, i.e. the presence of a ZnSe (surface) phase before etching and its removal upon HCl-treatment. The inset of Figure 10 shows the related detail spectra of the Se $3d_{3/2}$ and $3d_{5/2}$ spin-orbit split doublet, having a separation between 0.8 and 0.9 eV. The spectral shape of the Se 3d line significantly changes upon HCl etching. For the HCl-etched EVAP-$Cu_2ZnGeSe_4$ sample, the peak shape is attributed to the presence of (at least) two species. The main species (indicated with "M" in the inset; also dominating the spectrum of the as-deposited EVAP-$Cu_2ZnGeSe_4$ sample) is ascribed to a selenide, i.e., to selenium in a $Cu_2ZnGeSe_4$ and/or ZnSe environment – based

on the comparison of the Se 3d data with Ref. [12]. Based on this data it is not possible to unambiguously differentiate between ZnSe and $Cu_2ZnGeSe_4$. The low-intensity secondary species (indicated with "S" in the inset) that is responsible for the additional high-binding energy spectral intensity can most likely be explained by oxidized selenium (SeO_x, $x \geq 3$). However, note that due to the large spread of binding energy values found in published references [12], the presence of a germanium selenide binary phase (with Ge being in an oxidation state > 2+) and/or formation of Se-C bonds (in-line with the increased C signal) can also not be ruled out as an explanation for the high-binding energy Se 3d contribution. Whether and how this second Se species affects the chemical environment of additional $Cu_2ZnGeSe_4$ elements and/or the electronic structure of the absorber and how this is related to the observed solar cell characteristics is the topic of ongoing research. Work on the device level is in progress with the goal of developing a wet-chemical treatment to remove the HCl-etch induced formation of the second Se species in order to recover the FF and collection length, while keeping the V_{OC} gain resulting from HCl etching.

2.2.2. BUFFER LAYER DEVELOPMENT

The most widely used buffer layer for Cu chalcogenide thin film solar cells is CdS prepared by CBD. This preparation process results in a highly defect-rich material, also containing oxygen (OH) and carbon impurities [28]. Some of the properties of CBD-grown CdS (e.g. composition, defect nature, structure) depend on the experimental deposition parameters (concentration of the precursors, temperature of the chemical bath, etc.). Consequently, the CBD-CdS recipe needs to be adjusted for each absorber material for optimal solar cell performance. Hence, we empirically tuned the experimental parameters of the CdS deposition on the evaporated EVAP-$Cu_2ZnGeSe_4$ absorbers. We observe a V_{OC} increase with increasing deposition duration, accompanied with a decrease of FF and J_{SC} after a critical duration. More details about the buffer layer optimization, which resulted in a new record efficiency of 7.6 % for $Cu_2ZnGeSe_4$ based solar cells, can be found in Ref. [29].

Although it is the most-used buffer material for kesterite solar cells, CdS has a quite low optical band gap energy (2.4 eV) and high absorption coefficient for a material that would ideally be transparent. Consequently, there is a loss in current due to absorption of solar radiation in the CdS is in the range of 1-2 mA/cm². In case of a potential kesterite/Si tandem configuration, this loss would manifest in a 4 to 14 % relative decrease of the theoretically achievable J_{SC} [3]. Moreover, another important prerequisite to reach high efficiency is an ideal buffer/absorber interface that allows for lossless charge carrier transport without barriers for charge carriers and preventing high-rate charge carrier recombination routes. In order to systematically optimize the buffer/kesterite interface, we prepared solar cells based on wet-chemical deposited (see Section 2.1.2) 1.5 (+/- 0.05) eV band gap SOL-$Cu_2ZnGe(S,Se)_4$ absorbers (prepared according to the solution approach discussed in detail in Section 2.1.2)

and different buffer layer materials. The five different buffer materials used were: sputtered ("rf") $Zn(O_{0.6},S_{0.4})$, CBD-Zn(O,S), CBD-CdS, atomic layer chemical vapor deposited (ALCVD) In_2S_3, and co-evaporated ("co-evap.") $CdIn_2S_4$. A detailed discussion can be found in Ref. [17], briefly: Compared to the CdS reference, In_2S_3 and $Zn(O_{0.6},S_{0.4})$ buffers have a higher transmission, i.e., less absorption in the buffer layer (in the 350-500 nm wavelength range), as shown in Figure 11. Solar cells with $Zn(O_{0.6},S_{0.4})$ buffers also yield higher V_{OC} values. For these devices, a higher activation energy of the dominant recombination process was also derived (compared to the CdS reference) [17], strongly suggesting a more preferable electronic structure of the buffer/SOL-$Cu_2ZnGe(S,Se)_4$ interface. The sputtered-$Zn(O_{0.6},S_{0.4})$ buffered solar cells, however, achieve a lower overall efficiency, mainly due to reduced FF and J_{SC}, as presented in Table S1 [17]. We speculate that those losses originate from the nature of the deposition method, as all vacuum deposited buffer layers suffer from similar J_{SC} and FF losses, compared to solution-prepared CdS. For that reason, we also investigated wet-chemically deposited Zn(O,S) buffers. With CBD-Zn(O,S) buffers, SOL-$Cu_2ZnGe(S,Se)_4$ based solar cells achieve similar FF and J_{SC} values as the CdS reference, but lower V_{OC} values. A tentative explanation for this observation is the different composition of CBD-Zn(O,S) and sputtered-$Zn(O_{0.6},S_{0.4})$ buffers: certainly the O/S ratio, which determines the optical band gap of the Zn(O,S) material, can be different and the CBD-Zn(O,S) buffer may also contain oxide, hydroxide (OH), and/or carbon impurities, which can also have an impact on the optoelectronic properties. Additional work is in progress to optimize the CBD-Zn(O,S) buffer aiming at combining the good J_{SC} and FF values with the high V_{OC} that is obtained when sputtered-$Zn(O_{0.6}S_{0.4})$ is used as a buffer.

2.3. DEVICE SIMULATIONS

Numerical simulations were carried out using the SCAPS software [30] to determine the best device design for $Cu_2ZnGe(S,Se)_4$-based top cells in a tandem configuration, with a focus on suggesting suitable TBCs. The parameters used in the simulations are listed in Table S2 [31,32]. Most of the parameters related to the absorber material, such as thickness, doping concentration, band gap, and absorption coefficient, were extracted from (our own) electrical and optical measurements. Parameters related to $MoSe_2$ and MoO_3 were taken from literature, and those related to CdS and ZnO:Al layers are already available in the SCAPS software. Two configurations were tested in the simulations: $Cu_2ZnGe(S,Se)_4$ substrate or superstrate solar cells, as shown in Figure S5. In the standard configuration [substrate, Figure S5(a)], a thin layer of $MoSe_2$ was inserted in the model between the $Cu_2ZnGe(S,Se)_4$ absorber layer and the Mo contact. The presence of $MoSe_2$ layer at the absorber/Mo interface was previously reported for $Cu(In,Ga)Se_2$ [33] and $Cu_2ZnSnSe_4$ [34] TF solar cells. It was shown to be beneficial for TF solar cells performance if its thickness is controlled to avoid detrimental

effects on series resistance. The improvement of the solar cell performance is mainly due to a reduction of the barrier height and better charge carrier collection at the interface between the absorber and the Mo contact if $MoSe_2$ is present. For tandem cells, the Mo back contact needs to be replaced by a TBC, see Figure S5(b). However, most of the transparent conductive oxides (TCOs) used in solar cells have a low work function (4.7-4.9 eV [35]) and thus – if Anderson's rule holds true for these complex heterojunctions – may not result in a preferable energy level alignment with the $Cu_2ZnGe(S,Se)_4$ absorber layer when used as back contact. In this case, the use of an intermediate layer, such as a thin $MoSe_2$ or MoO_3, can mitigate this issue. MoO_x was successfully used in superstrate configuration as an interfacial layer between a transparent SnO_2:In (ITO) back contact and $Cu(In,Ga)Se_2$ absorbers [36] and was shown to also be a good interfacial layer for the $Cu_2ZnSnSe_4$ based solar cells (applied either as a layer between the absorber and the Mo contact to improve the back contact properties or as a primary back contact) [37-38].

Figure S6 shows the J(V) curves calculated for different device configurations. The solar cell parameters are given in Table 2. For the $Cu_2ZnGe(S,Se)_4$ substrate configuration (a), the calculated J(V) curve is based on series resistance and shunt resistance values of 4.7 and 365 Ωcm^2, respectively. These resistances have been extracted from the J(V) curve of one of the most efficient EVAP-$Cu_2ZnGeSe_4$ substrate solar cells (5.4 % power conversion efficiency). In the configurations (b)-(d), the J(V) curves were calculated after the (simulated) optimization of the absorber doping concentration (10^{16} cm^{-3}) and of the values for series and shunt resistance ($R_s \leq 0.5$ Ωcm^2; $R_{sh} \geq 800$ Ωcm^2). In case of a superstrate with TBC [configuration (c)], the low solar cell performance is due to a strong reduction of the V_{OC} caused by the low work function of ZnO:Al (AZO). The best configuration for superstrate solar cell was obtained by considering a thin "buffer layer" of MoO_3 between the absorber and a TCO back contact (d). It should be noticed that an ITO back contact acts also as a Na barrier. If insufficient Na content limits the device performance, however, Na needs to be deliberately added in a controlled way, e.g. by means of post-deposition treatment [39].

2.4. TRANSPARENT BACK CONTACTS

TBCs for potential use in the wide band gap $Cu_2ZnGe(S,Se)_4$ kesterite top cell of a four terminal photovoltaic tandem cell with a c-Si bottom cell have been studied. In addition to the electronic structure considerations in the previous section, the back contact must be transparent for photons with an energy below the band gap of the absorber layer and stable under its processing conditions. Independent of the processing route [evaporation-based (see Section 2.1.1) or solution-based (see Section 2.1.2.)], the kesterite absorber is formed by high-temperature annealing of the precursor layer stack in H_2Se and/or H_2S atmosphere. It is expected that this selenization/sulfurization will be the most critical processing step that the

TBC has to withstand. H_2Se is a more powerful reducing agent than is H_2S [40], and so we focus on the impact of annealing in H_2Se atmosphere on the optoelectronic and chemical properties of the TBCs in the following. The most widely used TCOs: ITO, AZO, and SnO_2:F (FTO) – were selected for exposure tests [41,42]. It is assumed that the S-containing atmosphere during annealing required to achieve the [S]/([S]+[Se]) composition necessary for the desired higher absorber band gap will have similar effects.

In order to simulate the impact of H_2Se exposure during a $Cu_2ZnGe(S,Se)_4$ deposition process, the optical and chemical properties of the selected TCOs have been tested before and after exposure to a 20 sccm H_2Se flow for 15 min at various treatment temperatures (400 and 450 °C). A first screening showed that ITO had the highest likelihood for yielding working devices but would require a protective top layer (to make it more stable during absorber processing). Furthermore, our SCAPS simulations (see Section 2.3) of $Cu_2ZnSn(S,Se)_4$ devices had shown that employing ITO instead of Mo (which is the standard back contact for single-junction devices) would result in an efficiency drop of 60 rel.% (see Table 2). The same simulations showed that this deterioration may be fully prevented by using an additional MoO_3 interlayer between ITO and absorber resulting even in an efficiency gain of 80 rel.% (see Table 2). Hence, thin sputtered MoO_3 layers applied on top of a 135-nm-thick sputtered ITO before absorber deposition – as protection layer and for improved energy level alignment – were first explored. However, MoO_3 is significantly reduced upon H_2Se exposure; in Section 2.4.1, we explore alternative protective layers.

2.4.1. PROTECTIVE TOP LAYERS

In this section, the effectiveness of Al_2O_3, $InZnO_x$ (IZO), and TiO_2 as protection of ITO during selenization/sulfurization is explored. The study is conducted by means of H_2Se exposure tests at 400°C and 450°C (i.e., annealing temperatures relevant for absorber formation), as well as by experiments on the device level. The top layers were deposited by means of atmospheric pressure spatial atomic layer deposition (S-ALD, plasma enhanced for IZO) [43].

2.4.1.1. LAYER PROPERTIES

Al_2O_3 is known to be an excellent passivation and barrier (i.e., protective layer) material of high chemical stability; it is however electrically insulating. IZO and TiO_2 are candidates for forming more conductive protective layers. In order to determine the minimum thickness for being a sufficient protective top layer and to test if such a thickness would yield a working device, a set of Al_2O_3 (1-30 nm), IZO (1-120 nm), and TiO_2 (2-60 nm) layers of different thicknesses were deposited by means of S-ALD on ITO coated SLG substrates. The absorption spectra (derived from reflectance and transmittance) shown in Figure 12 suggest that the decrease of ITO transmittance (i.e., increase of absorption) induced by H_2Se exposure could (to some degree) be prevented with a > 2 nm Al_2O_3 (not shown), > 30 nm IZO, or >

60 nm TiO_2 top layer. However, the TiO_2 layers are less effective at temperatures of 450°C and higher [see Figure 12(c)]. After H_2Se exposure at 450°C, the average absorption for an 135-nm-thick ITO layer with a 30-nm-thick IZO and 60-nm-thick TiO_2 protective layer is 8 and 18 %, respectively, in the near infra-red regime (between 750 nm and 1100 nm).

HAXPES was used for chemical structure analysis of the IZO/ITO back contact configuration and its changes upon H_2Se exposure in order to probe the deterioration of ITO and the protection mechanism of IZO. Note that same measurement conditions apply as for the HAXPES data shown in Figures 1 and 4. The Sn 3d XPS spectra of a bare ITO sample and ITO samples with either a 10 or a 30 nm protective IZO top layer before and after H_2Se treatment at 450 °C are shown in Figure 13. Before the H_2Se treatment, for the bare ITO and 10 nm IZO/ITO sample, Sn resides in a chemical environment best described by a combination of ITO, SnO, and SnO_2. However, note that asymmetric core level lines are generally found for (highly conductive) ITO and are generally attributed to final-state effects [44]. No Sn signal is observed for the 30 nm IZO/ITO sample, due to insufficient probing depth and complete coverage of the ITO by the IZO. (The inelastic mean free path of the Sn 3d photoelectrons excited with 6 keV photons in In_2O_3 is around 7 nm [45]). After H_2Se treatment, the spectral intensity of the Sn 3d line is significantly redistributed, indicating that the chemical environment of Sn has changed; SnSe and/or $SnSeO_x$ are likely present. Furthermore, the Sn 3d intensity increases after the H_2Se treatment for the 10 nm IZO/ITO sample, suggesting either that Sn diffuses into the IZO layer and/or the degree of ITO coverage decreases. If the protective layer does not completely cover the ITO, it will not prevent the chemical reaction between ITO and H_2Se, the evidence of which is the formation of Sn-Se bonds. Additional HAXPES data suggest a significant chemical interaction between IZO and H_2Se, implying that IZO acts as a sacrificial agent to protect ITO from H_2Se. Note that additional measurements on TiO_2/ITO test structures (not shown) reveal a different protection mechanism: TiO_2 is largely unaffected by H_2Se annealing.

2.4.1.2. SOLAR CELL DEVICES

EVAP-$Cu_2ZnGeSe_4$-based devices were manufactured on sputtered ITO/SLG substrates with S-ALD deposited Al_2O_3, IZO, and TiO_2 protective layers. As references, similarly prepared devices with a standard Mo back contact on a Si(O,N)/SLG substrate were also fabricated and tested. A CBD-CdS buffer and a sputtered i-ZnO/AZO bi-layer emitter was used as the front window. The (5×5 cm^2) EVAP-$Cu_2ZnGeSe_4$ cell stack samples were finished by applying a Ni/Ag grid for local J(V) measurements. Table 3 depicts measured J(V) parameters of the champion cells. As stated earlier, an Al_2O_3 thickness above 2 nm is needed for an effective H_2Se protection of ITO. However, the 3 nm thick Al_2O_3 layer used here already reduces the cell performance dramatically due to its insufficient conductivity. This issue could be overcome by using a perforated Al_2O_3 layer, which (through the formed point contacts) allows

sufficient charge carrier transport while also acting as a passivation and barrier layer. Devices with an ITO back contact with or without either a 30 nm TiO_2 or IZO protective top layer function better, yielding efficiencies of about 85-90 % of that of reference cells with a Mo back electrode. The lower efficiencies likely result from a higher sheet resistance of the back contact and a presumably less ideal energy level alignment at the absorber/back contact interface compared to the Mo back electrode. The combination of ITO back electrode with TiO_2 protection layer results in a higher V_{OC} than an ITO back electrode with or without IZO protection layer, but not in a higher J_{SC} value – finding an explanation for this observation is a subject of ongoing discussion.

Figure 14 depicts the absorption (derived from reflectance and transmittance) for a complete EVAP-$Cu_2ZnGeSe_4$ solar cell layer stack on a 60 nm TiO_2 protected ITO back electrode. The absorption of the complete cell stack for energies directly below E_G ($Cu_2ZnGeSe_4$) is 65 % for 60 nm TiO_2/ITO and 55 % for 30 nm IZO/ITO (not shown) back contacts. These values are higher than the sum computed from the absorption of the individual layers (i.e., back contact after H_2Se exposure, absorber, and front window), as illustrated in Figure 14 for the 60 nm TiO_2/ITO back contact. This may be due to slightly varying absorber layer deposition and/or selenization process conditions, annealing-induced formation of species at the absorber (precursor)/TBC interface, or internal reflections and higher absorption of the front window when deposited on the actual (rough) absorber layer. In order to reduce the optical losses in a complete device, more analysis of the composition and morphology of the layers and their interfaces in the cell stack will be needed. To reduce near-infrared absorption due to free charge carriers in both the highly-doped back and front contact, more effort is required to develop transparent materials with high mobilities and reasonable charge carrier densities.

3. OUTLOOK

The bottom cell in a tandem configuration will only receive the illumination transmitted through the top cell, and so a good transmission at $h\nu <$ than the top cell absorber band gap is crucial for the top cell structure to successfully be employed in tandem configurations, as discussed in the previous section. A thin top cell combined with a TBC is generally used to assure this. To investigate the effect of the top cell transparency on the performance of the bottom cell (c-Si), we calculated the efficiency of the bottom cell as a function of the light transmitted through the top cell, as shown in Figure 15. The bottom cell is modeled as a 25 % efficient silicon cell with rear locally diffused contacts (PERL technology [46]) and Lambertian light trapping [47-48]. For the tandem cell, a four-terminal mechanically stacked configuration is considered. In Figure 15, the efficiency of the c-Si bottom cell under the absorbing 1.5 eV band gap $Cu_2ZnGe(S,Se)_4$-based cell is shown as a function of top cell

transmission. Furthermore, the total efficiency of the tandem configuration assuming a top cell efficiency of 8, 15, and 22 % is shown. In the case of a $Cu_2ZnGe(S,Se)_4$(1.5 eV)-based top cell of 8 % efficiency (i.e., a performance level similar to the one reached as a result of joint research efforts of this consortium, see Section 2.2.2), a transparency higher than 80 % is required to achieve a total tandem device efficiency that is higher than the efficiency of the c-Si bottom cell alone (25 %, horizontal dashed line in Fig. 21). In case the efficiency of the top cell can be increased to 15 % (a performance level that seems feasible based on our device simulation in Section 2.3, see Table 2), a transparency above 50 % is sufficient for viable tandem application. Finally, for a 22 % efficient top cell (a performance level that has been shown for other polycrystalline chalcogenide-based absorbers [2]) respective tandem devices would reach efficiencies > 25% with even more relaxed top cell transparency requirements.

A maximal transparency of approximately 40 % for a real-world $Cu_2ZnGe(S,Se)_4$/TBC layer stack was shown in this contribution (see Fig. 20 and discussion in Section 2.4.1.2); there is a realistic potential to increase this to 60 % if chemical reactions at the interfaces and/or internal reflections can be minimized. Hence, wide band gap kesterites might very well represent a material class that may be used as absorber in tandem device top cells if further significant advancements in cell performance (8 → 15%) and transmission (40 → 60%) are achieved. Based on the progress presented in this paper (compare status 2015 and 2018 indicated as ❶ and ❷ in Figure 15), it indeed seems feasible to reach the realistic performance scenario (❸ in Figure 15) if optimization efforts continue.

4. CONCLUSIONS

Absorbers in which Sn had been substituted by Si did not result in functioning solar cells; most likely due to too high doping (in the order of 10^{18} cm^{-3}) and/or the formation of SiO_2 at the absorber surface. However, $Cu_2ZnGe(S,Se)_4$ absorbers with band gaps above 1.5 eV have been successfully developed and integrated into solar cells. Typically, ZnSe is present in large amounts on the top surface of these absorbers; it is shown here that this impurity can be selectively removed with chemical etching: (i) with 12 wt% HCl at a temperature of 60-85 °C, and (ii) in 1M $KMnO_4$ / 1M H_2SO_4 aqueous solution. The standard CBD-CdS has been optimized, resulting in a record efficiency of 7.6 % for EVAP-$Cu_2ZnGeSe_4$ based solar cells (with Mo back contact). In_2S_3, Zn(O,S), and $CdIn_2S_4$ alternative buffer layers were also tested, where the highest V_{OC} and presumably the best electronic buffer/absorber interface structure could be obtained with sputtered Zn(O,S).

The solar cell performance of substrate/superstrate $Cu_2ZnGe(S,Se)_4$ solar cells with TBC for tandem application was simulated using SCAPS to evaluate various configurations and identify performance-limiting factors. It was found that when low work function, TCO-based, TBCs

(like ITO) are used, an "interlayer" is required to reduce the blocking barrier at the absorber/TCO interface, ideally achieving an Ohmic contact. The device simulation suggests MoO_x as an ideal interlayer candidate material for $Cu_2ZnGe(S,Se)_4$ superstrate cells for tandem applications. MoO_x is, however, unstable under real-world absorber processing conditions; the use of an alternative, stable material causes the majority of respective (transparent) cells to be still limited by a low V_{OC}.

ITO was shown to be a well-performing candidate for a TBC, but it requires a protective top layer (i.e., Al_2O_3, IZO, or TiO_2) if it is to remain transparent after exposure to the Se (and/or S) atmosphere needed for the absorber deposition process. ITO back contacts with a protective layer of 30-nm-thick IZO or 60-nm-thick TiO_2 have an average absorption of 8 and 18 %, respectively, in the near infra-red regime. The efficiency of solar cells using an ITO with IZO or TiO_2 protective layers achieves 85-90 % of the performance of reference cells with Mo back contact (at a maximal transparency of 40 %).

In summary, $Cu_2ZnGe(S,Se)_4$ absorbers with potential for future application as top cell in tandem configurations have been developed. Different optimization routes mostly addressing the buffer/absorber interface have been suggested and proven to be effective to advance device performance. In order to make wide band gap kesterites a prime candidate absorber material for the top cell in tandem devices, similar approaches are crucially needed extending the efforts to all aspects of the complete cell stack, tackling interface *and* bulk properties in order to improve cell efficiency and transmission. In order to accomplish this challenge, it is proposed to focus future research on increasing the solar cell performance before addressing the transparency of these solar cell devices.

ACKNOWLEDGEMENTS

This project has received funding from the European Union's Horizon 2020 research and innovation program under grant agreement N° 640868. The synchrotron radiation experiments were performed at the SPring-8 beamline BL15XU with the approval of the NIMS Synchrotron X-ray Station (Proposals 2016A4600, 2016B4601, and 2017A4600) and at BESSY II with the approval of HZB. B. Vermang has received funding from the European Research Council (ERC) under the European Union's Horizon 2020 research and innovation programme (grant agreement n° 715027).

REFERENCES

[1] M.A. Green, S. Hishikawa, E.D. Dunlop, D.H. Levi, J. Hohl-Ebinger, A.W.Y. Ho-Baillie, Prog. Photovoltaics Res. Appl., 2018, **26**, 3-12.

[2] Solar Frontier Achieves World Record Thin-Film Solar Cell Efficiency of 22.9 %, Solar Frontier press release, http://www.solar-frontier.com/eng/news/2017/1220_press.html, last accessed May 23rd 2018.

[3] W. Shockley, H.J. Queisser, J. Appl. Phys., 1961, **32**, 510-519.

[4] T.P. White, N.N. Lal, K.R. Catchpole, IEEE J. Photovoltaics, 2014, **4**, 208-214.

[5] T.K. Todorov, D.M. Bishop, Y. Seog Lee, Sol. Energy Mater. Sol. Cells, 2018, **180**, 350-357.

[6] S. Siebentritt, S. Schorr, Prog. Photovoltaics Res. Appl., 2012, **20**, 512-519.

[7] W. Wang, M.T. Winkler, O. Gunawan, T. Gokmen, T.K. Todorov, Y. Zhu, D.B. Mitzi, Adv. Energy Mater., 2014, **4**, 1301465.

[8] M. León, S. Levcenko, R. Serna, G. Gurieva, A. Nateprov, J.M. Merino, E. J. Friedrich, U. Fillat, S. Schorr, E. Arushanov, J. Appl. Phys., 2010, **108**, 093502.

[9] Q. Shu, J.-H. Yang, S. Chen, B. Huang, H. Xiang, X.-G. Gong, S.-H. Wei, Phys. Rev. B, 2013, **87**, 115208.

[10] G. Brammertz, B. Vermang, H. Elanzeery, S. Sahayaraj, S. Ranjbar, M. Meuris, J. Poortmans, Thin Solid Films, 2016, **616**, 649-654.

[11] G. Brammertz, B. Vermang, H. Elanzeery, S. Sahayaraj, S. Ranjbar, M. Meuris, J. Poortmans, Phys. Status Solidi C, 2017, **14**, 1600162.

[12] NIST X-ray Photoelectron Spectroscopy Database, version 3.5, National Institute of Standards and Technology, Gaithersburg, 2003, https://srdata.nist.gov/xps/, last accessed May 23rd 2018.

[13] G. Brammertz, B. Vermang, M. Meuris, J. Poortmans, Thin Solid Films, 2019, **670**, 76-79.

[14] T. Schnabel, M. Seboui, E. Ahlswede, RSC Adv., 2016, **7**, 26-30.

[15] S. Ueda, Y. Katsuya, M. Tanaka, H. Yoshikawa, Y. Yamashita, S. Ishimaru, Y. Matsushita, K. Kobayashi, AIP Conference Proceedings, 2010, **1234**, 403-406.

[16] S. Ueda, J. Electron Spectrosc. Relat. Phenom., 2013, **190 Part B**, 235-241.

[17] T. Schnabel, M. Seboui, L. Choubrac, L. Arzel, S. Harel, N. Barreau, E. Ahlswede, RSC Adv., 2017, **7**, 40105-40110.

[18] M. Werner, D. Keller, S.G. Haass, C. Gretener, B. Bissig, P. Fuchs, F. La Mattina, R. Erni, Y.E. Romanyuk, A.N. Tiwari, ACS Appl. Mater. Interfaces, 2015, **7**, 12141-12146.

[19] T. Gershon, K. Sardashti, O. Gunawan, R. Mankad, S. Singh, Y.S. Lee, J.A. Ott, A. Kummel, R. Haight, Adv. Energy Mater., 2016, **6**, 1601182.

[20] J. Ge, Y. Yu, Y. Yan, ACS Energy Lett., 2016, **1**, 583-588.

[21] Y. Zhang, J.R.G. Evans, S. Yang, Journal of Chemical & Engineering Data, 2011, **56**, 328-337.

[22] T. Schnabel, M. Seboui, E. Ahlswede, Energies, 2017, **10**, 1813.

[23] J. Chen, W. Li, C. Yan, S. Huang, X. Hao, J. Alloys Compd., 2015, **621**, 154-161.

[24] M. Kumar, A. Dubey, N. Adhikari, S. Venkatesan, and Q. Qiao, Energy Environ. Sci., 2015, **8**, 3134-3159.

[25] E.M. Gavrishchuk, E.Y. Vilkova, O.V. Timofeev, U.P. Borovskikh, E.L. Tikhonova, Inorg. Mater., 2007, **43**, 579-583.

[26] S. López-Marino, Y. Sánchez, M. Placidi, A. Fairbrother, M. Espindola-Rodríguez, X. Fontané, V. Izquierdo-Roca, J. López-García, L. Calvo-Barrio, A. Pérez-Rodríguez, E. Saucedo, Chemistry: A European Journal, 2013, **19**, 14814-14822.

[27] S. Bourdais, C. Choné, B. Delatouche, A. Jacob, G. Larramona, C. Moisan, A. Lafond, F. Donatini, G. Rey, S. Siebentritt, A. Walsh, G. Dennler, Adv. Energy Mater., 2016, **6**, 1502276.

[28] P. O'Brien, J. McAleese, J. Mater. Chem., 1998, **8**, 2309-2314.

[29] L. Choubrac, G. Brammertz, N. Barreau, L. Arzel, S. Harel, M. Meuris, B. Vermang, Phys. Status Solidi A, 2018, **215**, 1800043.

[30] M. Burgelman, K. Decock, S. Khelifi, A. Abass, Thin Solid Films, 2013, **535**, 296-301.

[31] A. Jäger-Waldau, M.Ch. Lux-Steiner, R. Jäger-Waldau, E. Bucher, Springer Proceedings in Physics, Polycrystalline Semiconductors II, 1991, **54**, 397-402.

[32] H. Simchi, B.E. McCandless, T. Meng, J.H. Boyle, W.N. Shafarman, J. Appl. Phys., 2013, **114**, 013503.

[33] D. Abou-Ras, G. Kostorz, D. Bremaud, M. Kälin, F.V. Kurdeseau, A.N. Tiwari, M. Döbeli, Thin Solid Films, 2005, **480-481**, 433-438.

[34] B. Shin, Y. Zhu, N.A. Bojarczuk, S. J. Chey, S. Guha, Appl. Phys. Lett., 2012, **101**, 053903.

[35] A. Klein, C. Körber, A. Wachau, F. Säuberlich, Y. Gassenbauer, S.P. Harvey, D.E. Proffit, T.O. Mason, Materials, 2010, **3**, 4892-4914.

[36] H. Simchi, J.K. Larsen, K. Kim, W. Shafarman, IEEE J. Photovoltaics, 2014, **4**, 1630-1635.

[37] S. Lopez-Marino, M. Espindola-Rodriguez, Y. Sanchez, X. Alobé, F. Olivia, H. Xie, M. Neuschitzer, S. Giraldo, M. Placidi, R. Caballero, V. Izquierdo-Roca, A. Pérez-Rodriguez, E. Saucedo, Nano Energy, 2016, **26**, 708-721.

[38] J. Park, J. Huang, K. Sun, Z. Ouyang, F. Liu, C. Yan, H. Sun, A. Pu, M. Green, X. Hao, Thin Solid Films, 2018, **648**, 39-45.

[39] D. Rudmann, A.F.d. Cunha, M. Kaelin, F. Kurdesau, H. Zogg, A.N. Tiwari, G. Bilger, Appl. Phys. Lett., 2004, **84**, 1129-1131.

[40] S. Oae, J.T. Doi, Heteroat. Chem, 1991, **4**, 531.

[41] I. Volintiru. A. de Graaf, J. van Deelen, P. Poodt, Thin Solid Films, 2011, **519**, 6258-6263.

[42] J. van Deelen, A. Illiberi, B. Kniknie, H. Steijvers, A. Lankhorst, P. Simons, Surf. Coat. Technol., 2013, **230**, 239-244.

[43] P. Poodt, D.C. Cameron, E. Dickey, S.M. George, V. Kuznetsov, G.N. Parsons, F. Roozeboom, G. Sundaram, A. Vermeer, J. Vac. Sci. Technol., A, 2012, **30**, 010802.

[44] C. Körber, V. Krishnakumar, A. Klein, G. Panaccione, P. Torelli, A. Walsh, J.L.F. Da Silva, S.-H. Wei, R.G. Egdell, D.J. Payne, Phys. Rev. B, 2010, **81**, 165207.

[45] H. Shinotsuka, S. Tanuma, C.J. Powell, D.R. Penn, Surf. Interface Anal., 2015, **47**, 871-888.

[46] J. Zhao, A. Wang, P.P. Altermatt, S.R. Wenham, M.A. Green, Sol. Energy Mater. Sol. Cells, 1996, **41-42**, 87-99.

[47] M.A. Green, Prog. Photovoltaics Res. Appl., 2009, **17**, 183-189.

[48] S. Khelifi, J. Verschraegen, M. Burgelman, A. Belghachi, Renewable Energy, 2008, **33**, 293-298.

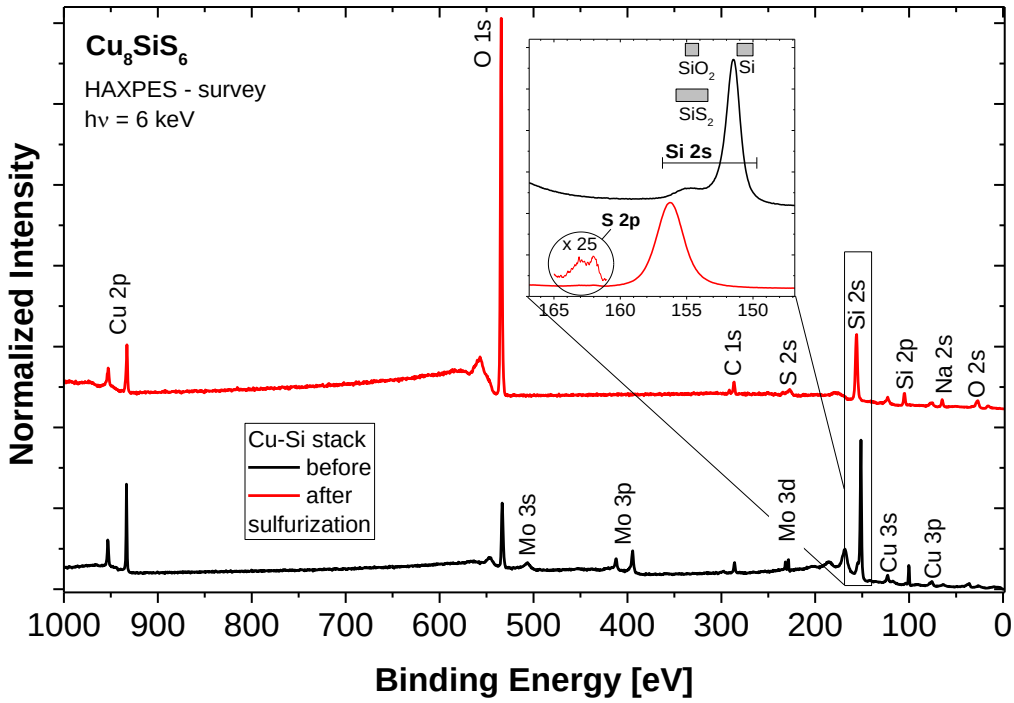

Figure 1: Hard x-ray photoelectron survey spectra of an EVAP-Cu_8SiS_6 sample before (black) and after (red) sulfurization treatment (spectra are offset for clarity). Due to the sulfurization, the oxygen and sodium (most likely diffused from the soda-lime glass substrate) contents increase. The inset shows the region of the Si 2s and S 2p core level lines compared to reference positions [12] of silicon compounds (note that the order of appearance is different compared to the survey spectra for better visibility). The S 2p line can only be clearly observed on a magnified (x 25) scale.

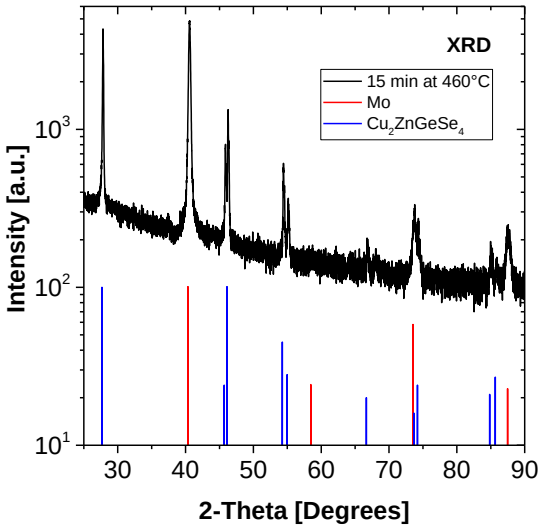

Figure 2: X-ray diffraction pattern of the EVAP-$Cu_2ZnGeSe_4$ absorber layer fabricated by selenizing the precursor stack for 15 min at 460°C on a Mo back contact together with reference positions for $Cu_2ZnGeSe_4$ and Mo (PDF card 00-052-0867).

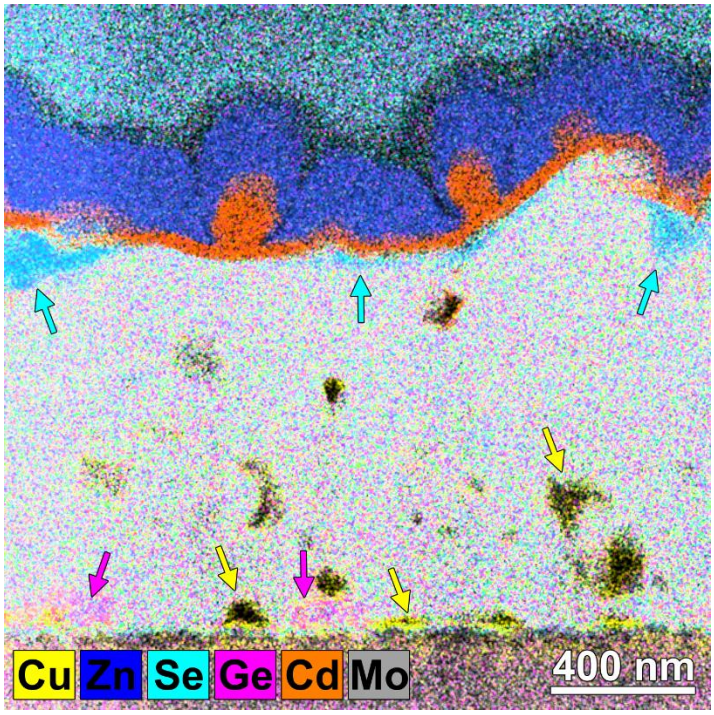

Figure 3: Cross-section STEM-EDX elemental map of a complete EVAP-$Cu_2ZnGeSe_4$ solar cell sample with CdS buffer layer and ZnO window, showing in some regions inhomogeneous elemental distributions, most likely caused by secondary phases. Regions attributed to ZnSe- (blue arrows), Cu_2GeSe_3- (pink arrows), and $Cu_{2-x}Se$-like (yellow arrows) phases are indicated. See also [13].

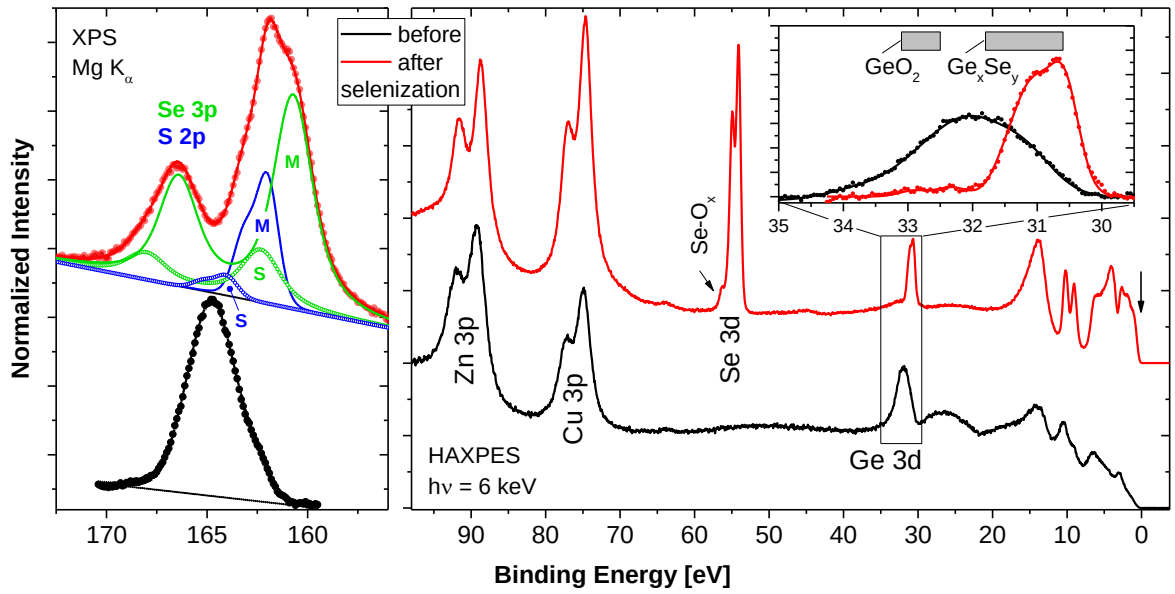

Figure 4: XPS (left panel) and HAXPES (right panel) S 2p/Se 3p and shallow core level spectra, respectively, of a SOL-$Cu_2ZnGe(S,Se)_4$ absorber before (black) and after (red) Se-annealing induced absorber formation (spectra are offset for clarity). For the S 2p / Se 3p spectrum of the sample after selenization the respective fits of the S 2p (blue) and Se 3p (green) doublets are also shown. (M – main species, S – secondary species). The inset in the right panel shows the region of the Ge 3d shallow core level compared to reference positions for germanium compounds [12].

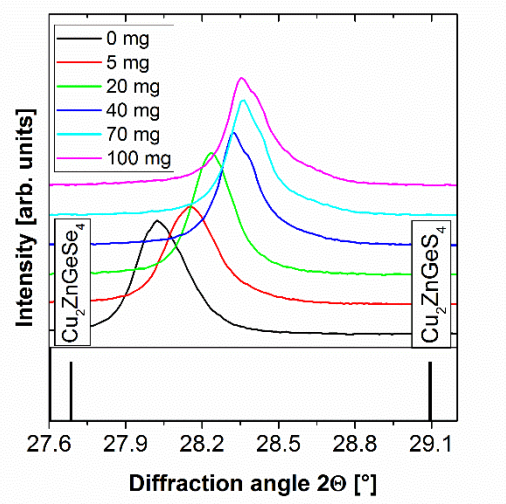

Figure 5: 112-reflection of XRD patterns from SOL-$Cu_2ZnGe(S,Se)_4$ absorbers processed in the presence of different amounts of GeS (0-100 mg).

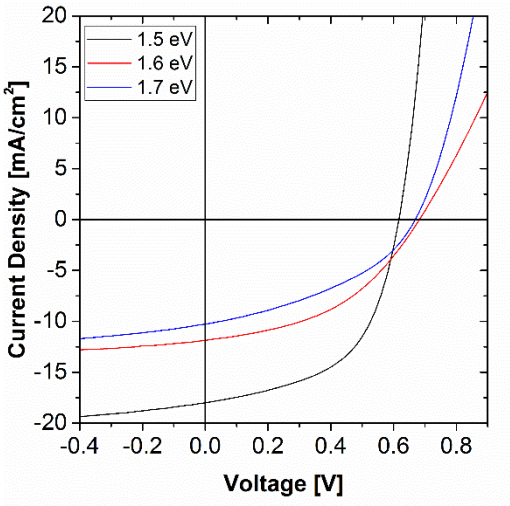

Figure 6: J(V)-characteristics of the best solar cells that were prepared from SOL-$Cu_2ZnGe(S,Se)_4$ absorbers with band gaps of 1.5, 1.6, and 1.7 eV, respectively, as determined from EQE. The corresponding [S]/([S]+[Se])-ratios are 0.27, 0.39, and 0.50.

E_G (eV)	1.5	1.6	1.7
Eff. (%)	6.0	3.6	2.7
V_{OC} (mV)	617	683	669
J_{SC} (mA/cm^2)	18.0	11.9	10.3
FF (%)	54.1	44.1	39.7

Table I: Solar cell parameters of solar cells with SOL-$Cu_2ZnGe(S,Se)_4$ absorbers with band gaps of 1.5, 1.6, and 1.7 eV, respectively.

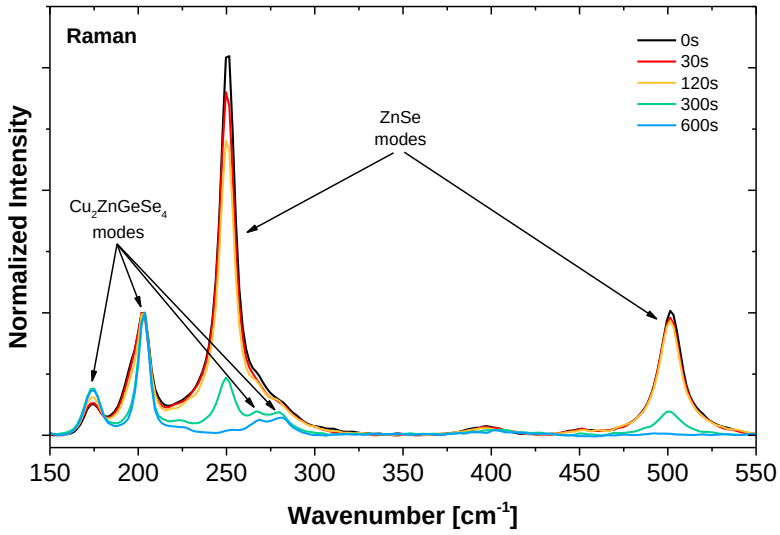

Figure 7: Raman spectra recorded with an excitation wavelength of 458 nm of EVAP-$Cu_2ZnGeSe_4$ samples that underwent HCl etching (T = 75°C, 12 wt% HCl) for different durations (from 0 to 600 s). Intensities are normalized to the most intense $Cu_2ZnGeSe_4$ peak (≈ 204 cm^{-1}).

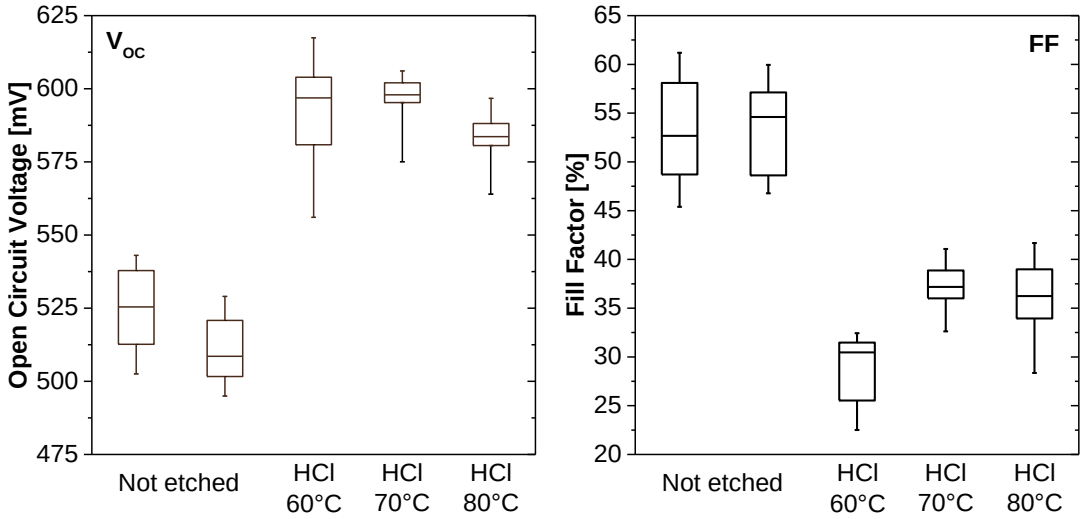

Figure 8: V_{OC} and FF mean values of EVAP-$Cu_2ZnGeSe_4$ based solar cells prepared using not-etched absorbers and absorbers HCl etched (using a 12 wt% HCl solution) at different temperatures (60 min a 60°C, 40 min at 70°C, 15 min at 80°C; 8-12 cells per sample, solar cell area ≈ 0.5 cm²).

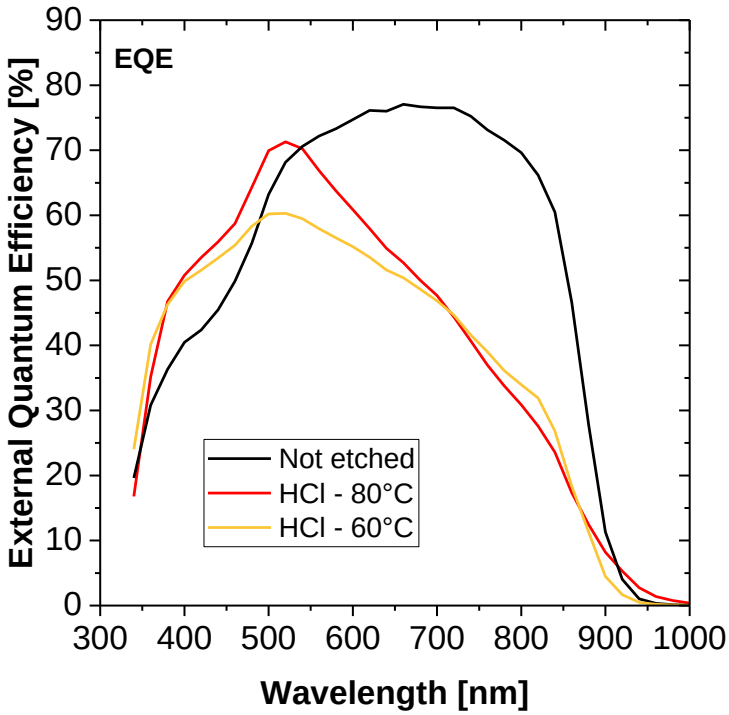

Figure 9: Representative EQE spectra of EVAP-$Cu_2ZnGeSe_4$ solar cells based on not-etched absorbers and absorbers HCl etched (using a 12 wt% HCl solution) at different temperatures (60 min a 60°C, 15 min at 80°C).

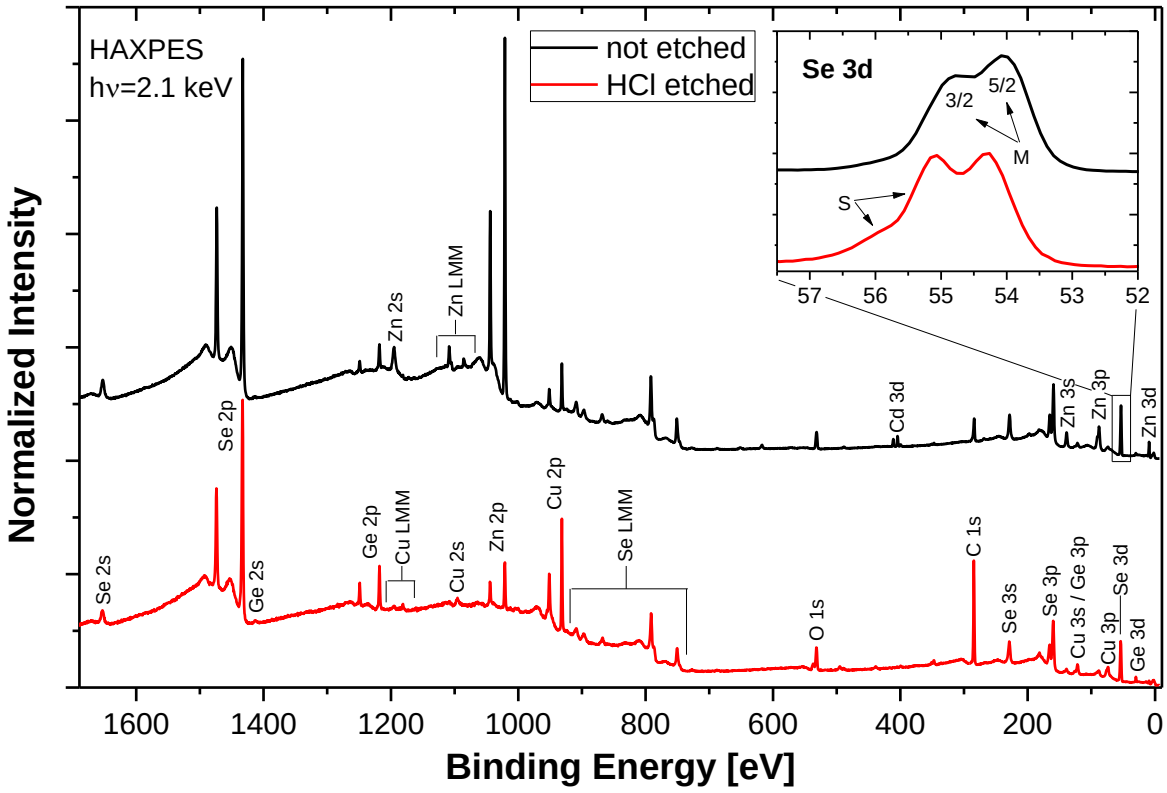

Figure 10: HAXPES survey spectra of an as-deposited / not etched (black spectrum) and HCl etched (red spectrum) EVAP-$Cu_2ZnGeSe_4$ absorber. Spectra are offset for clarity and all prominent lines are labelled. Inset: Detail spectra of the related Se 3d energy region, with the 3/2 and 5/2 spin-orbit split doublet indicated. Further, the approximate positions of the Se $3d_{3/2}$ and $3d_{5/2}$ lines of the main ("M") and secondary ("S") selenium species are depicted.

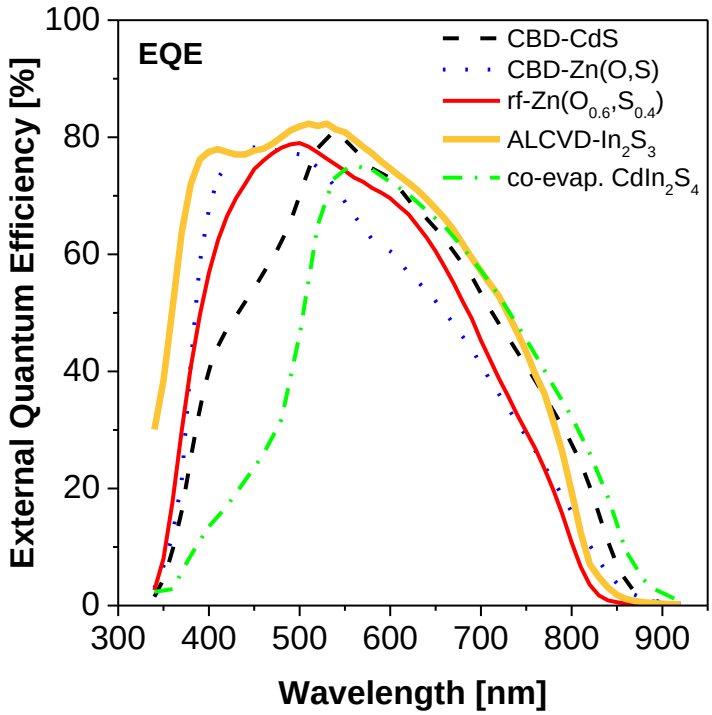

Figure 11: Representative EQE spectra of solar cells with SOL-$Cu_2ZnGe(S,Se)_4$ absorber and different buffer layers: sputtered (rf) $Zn(O_{0.6},S_{0.4})$, CBD-Zn(O,S), CBD-CdS, atomic layer chemical vapor deposited (ALCVD) In_2S_3, and co-evaporated ("co-evap.") $CdIn_2S_4$.

	Cell configurations			
Solar cell parameters	(a)	(b)	(c)	(d)
Back contact	$MoSe_2$/Mo	$MoSe_2$/Mo$^{(O)}$	TCO $^{(O)}$	MoO_3/TCO$^{(O)}$
V_{OC} (mV)	553	572	287	1000
J_{SC} (mA/cm^2)	19.70	20.00	17.60	22.00
FF (%)	56.30	71.00	65.54	67.90
Eff. (%)	6.22	8.14	3.31	15.00

Table 2: Solar cell parameters calculated for the different configurations as derived from the J(V) data shown in Figure S6. $^{(O)}$ Results from device simulation employing optimized parameters (see Table S2).

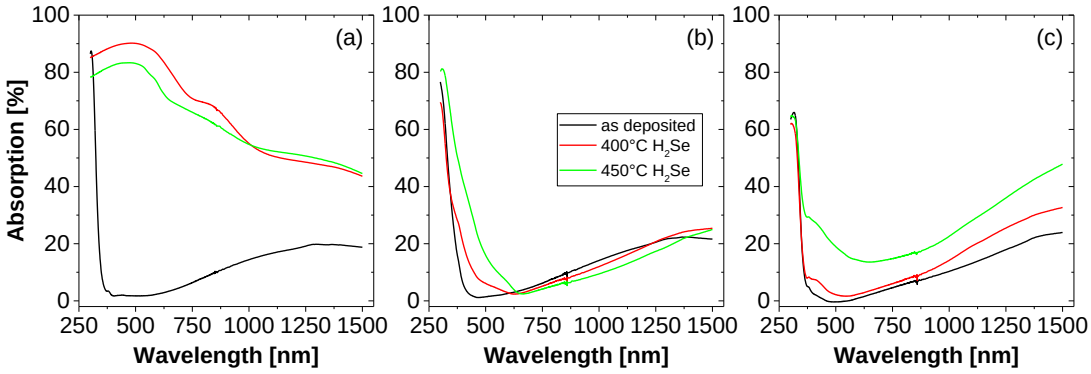

Figure 12: Absorption of ITO without (a) and with a 30 nm IZO (b), and with a 60 nm TiO_2 (c) protective top layer before (i.e., as-deposited) and after H_2Se exposure at 400 and 450°C.

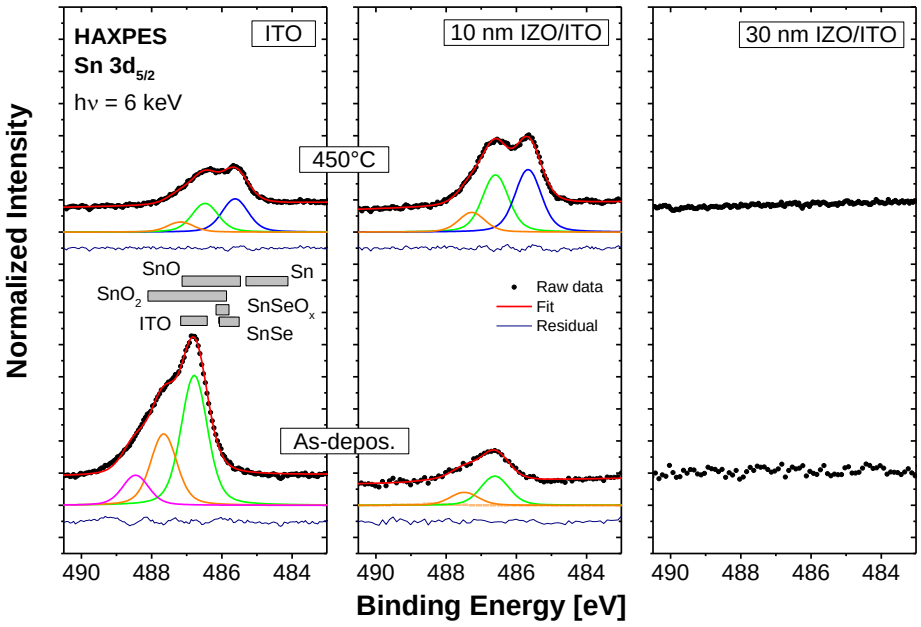

Figure 13: Sn $3d_{5/2}$ HAXPES spectra of the ITO, 10 nm, and 30 nm IZO/ITO samples before ("As-depos.") and after H_2Se treatment at 450 °C. The curve fit was done by using one linear background and three Voigt profiles. The grey boxes indicate the Sn $3d_{5/2}$ energetic position for reference compounds [12].

Back contact	Protective top layer	$Eff._{max}$ (%)	J_{SC} (mA/cm^2)	V_{OC} (mV)	FF (%)
ITO	None	3.6	19.9	487	37.6
ITO	IZO (30 nm)	4.0	27.1	471	31.2
ITO	Al_2O_3 (3.5 nm)	0.8	9.3	364	23.9
ITO	TiO_2 (30 nm)	4.3	17.3	600	41.3
SiON/Mo	None	4.7	18.6	600	42.3

Table 3: Overview of the J(V) parameters of the manufactured EVAP-$Cu_2ZnGeSe_4$ devices (best cells).

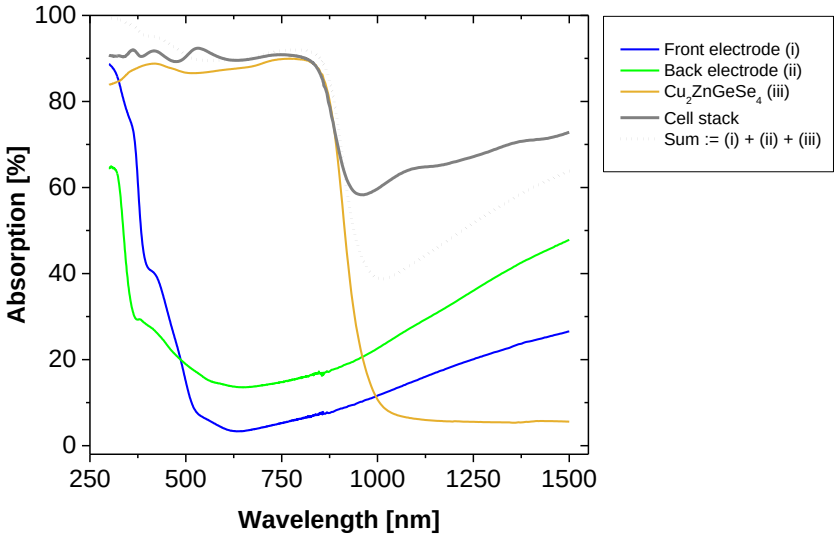

Figure 14: Absorption spectra of the (complete) front electrode/EVAP-$Cu_2ZnGeSe_4$/60 nm TiO_2/ITO cell stack and of the individual stack components: (i) ZnO:Al front electrode, (ii) 60 nm TiO_2/ITO back electrode after H_2Se exposure at 450°C, (iii) EVAP-$Cu_2ZnGeSe_4$ absorber (as-deposited on quartz glass substrate) compared to their spectral sum := (i) + (ii) + (iii).

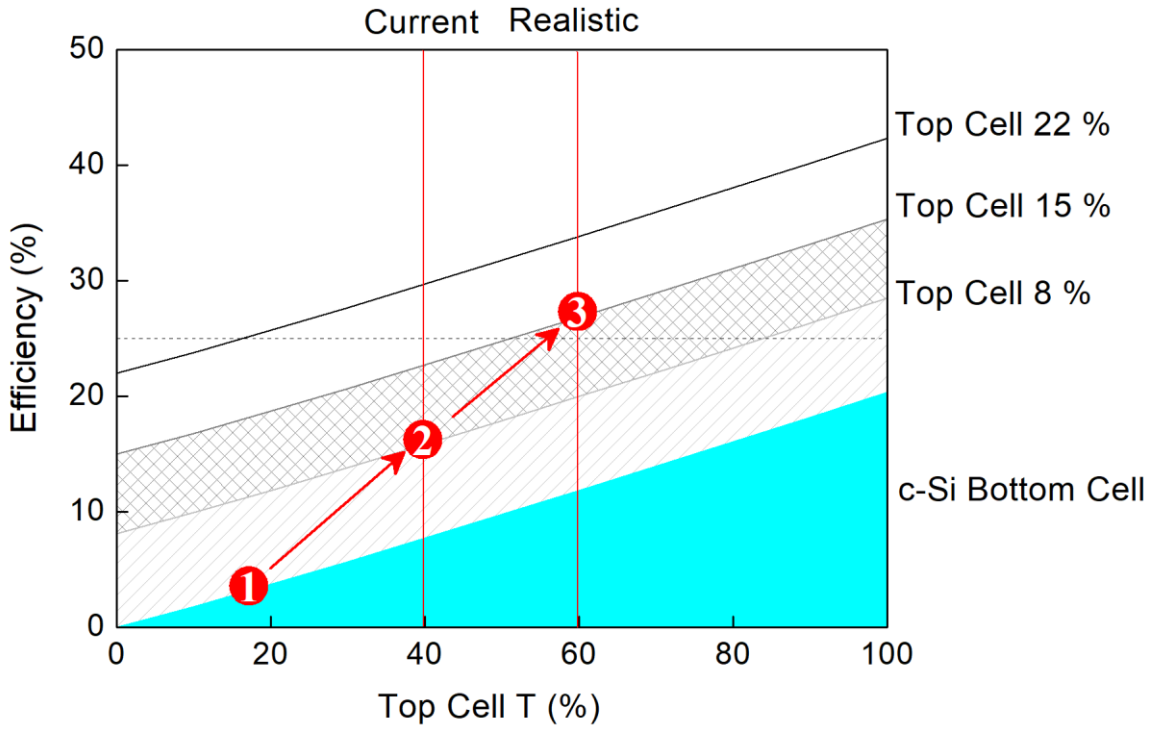

Figure 15: The efficiency of a four-terminal mechanically stacked geometry c-Si bottom+top cell as function of the light transmitted through the top cell (T for $\lambda \geq hc/Eg_{Top}$). As top cell, 8 and 15 % CZGSe and 22 % CIGS cells are used. The horizontal dashed line indicates the efficiency of the c-Si bottom cell alone and serves as a performance reference. ❶ and ❷ indicate the performance situation in 2015 ($\eta \approx 3$ % and T ≈ 17 %, calculated for measured transparency of CZGSe on TBC (ITO/TiO_2)) and 2018 (as reported in this publication: $\eta \approx$ 8 % and T ≈ 40 %). ❸ indicates a realistic performance scenario for which η and T have to be increased to 15 % and 60 %, respectively.

SUPPLEMENTARY MATERIAL FOR

WIDE BAND GAP KESTERITE ABSORBERS FOR THIN FILM SOLAR CELLS: POTENTIAL AND CHALLENGES FOR THEIR DEPLOYMENT IN TANDEM DEVICES

Bart Vermang[1,2,3], Guy Brammertz[1,2,3], Marc Meuris[1,2,3], Thomas Schnabel[4], Erik Ahlswede[4], Leo Choubrac[5], Sylvie Harel[5], Christophe Cardinaud[5], Ludovic Arzel[5], Nicolas Barreau[5], Joop van Deelen[6], Pieter-Jan Bolt[6], Patrice Bras[7], Yi Ren[7], Eric Jaremalm[7], Samira Khelifi[8,9], Sheng Yang[8], Johan Lauwaert[8], Maria Batuk[10], Joke Hadermann[10], Xeniya Kozina[11], Evelyn Handick[11], Claudia Hartmann[11], Dominic Gerlach[12], Asahiko Matsuda[13], Shigenori Ueda[14,15], Toyohiro Chikyow[12,13], Roberto Félix[11], Yufeng Zhang[11,16], Regan G. Wilks[11,17], and Marcus Bär[11,17,18,19]

[1]imec division IMOMEC – partner in Solliance, Wetenschapspark 1, 3590 Diepenbeek, Belgium

[2]Hasselt University – partner in Solliance, Martelarenlaan 42, 3500 Hasselt, Belgium

[3]EnergyVille, Thorpark 8320, 3600 Genk, Belgium

[4]ZSW, Meitnerstrasse 1, 70563 Stuttgart, Germany

[5]Institut des Matériaux Jean Rouxel (IMN), Université de Nantes, CNRS, 2 rue de la Houssinière, 44322 Nantes, France

[6]TNO – partner in Solliance, High Tech Campus 21, 5656 AE Eindhoven, The Netherlands

[7]Midsummer AB, Elektronikhöjden 6, 175 43 Järfälla, Sweden

[8]Department of Electronics and Information Systems (ELIS), Ghent University, Technologiepark Zwijnaarde 15, 9052 Gent, Belgium

[9]Department of Solid State Sciences, Ghent University, Krijgslaan 281-S1, 9000 Gent, Belgium

[10]Electron Microscopy for Materials Science (EMAT), University of Antwerp, Groenenborgerlaan 171, 2020 Antwerp, Belgium

[11]Department Interface Design, Helmholtz-Zentrum Berlin für Materialien und Energie GmbH (HZB), Hahn-Meitner-Platz 1, 14109 Berlin, Germany

[12]International Center for Materials Nanoarchitectonics (MANA), National Institute for Materials Science (NIMS), 1-1 Namiki, Tsukuba, Ibaraki 305-0044, Japan

[13]Research and Services Division of Materials Data and Integrated System (MaDIS), National Institute for Materials Science (NIMS), 1-1 Namiki, Tsukuba, Ibaraki 305-0044, Japan

[14]Synchrotron X-ray Station at SPring-8, National Institute for Materials Science (NIMS), 1-1-1 Kouto, Sayo-cho, Hyogo 679-5148, Japan

[15]Research Center for Advanced Measurement and Characterization, National Institute for Materials Science (NIMS), 1-2-1, Sengen, Tsukuba, Ibaraki 305-0047, Japan

[16]College of Physical Science and Technology, Xiamen University (XMU), 361005, Xiamen, China

[17]Energy Materials In-Situ Laboratory Berlin (EMIL), Helmholtz-Zentrum Berlin für Materialien und Energie GmbH (HZB), Albert-Einstein-Str. 15, 12489, Berlin, Germany

[18]Department of Chemistry and Pharmacy, Friedrich-Alexander-Universität Erlangen-Nürnberg, 91058 Erlangen, Germany

[19]Helmholtz-Institute Erlangen-Nürnberg for Renewable Energy (HI ERN), 12489 Berlin, Germany

CORRESPONDING AUTHOR – Bart Vermang, Martelarenlaan 42, 3500 Hasselt, Belgium

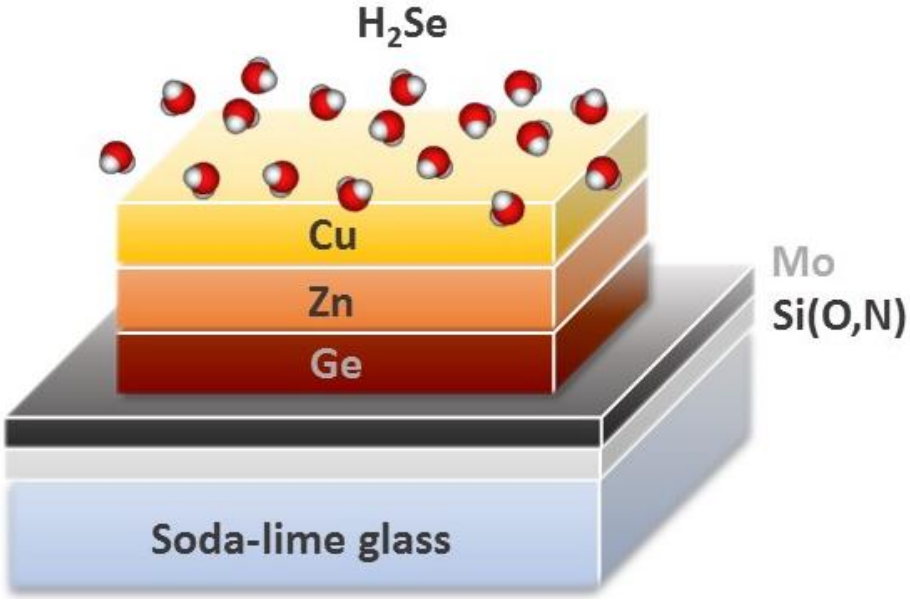

Figure S1: Schematic representation of the two-step selenization process used for EVAP-$Cu_2ZnGeSe_4$ absorber fabrication.

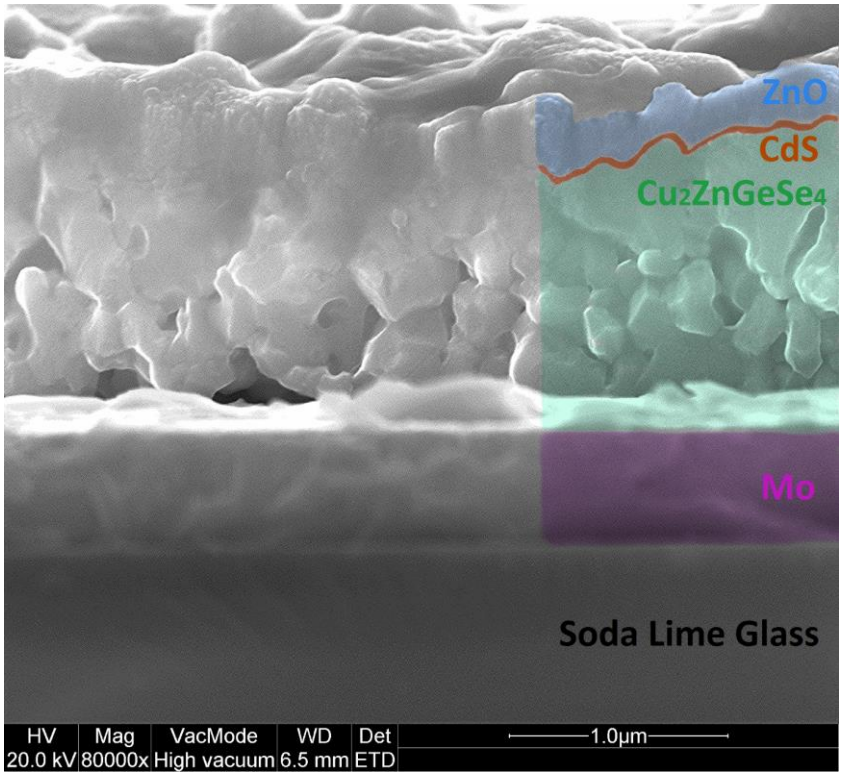

Figure S2: Cross-section scanning electron microscopy image of a finished EVAP-$Cu_2ZnGeSe_4$ solar cell sample, showing the grain morphology of the absorber and contact layer.

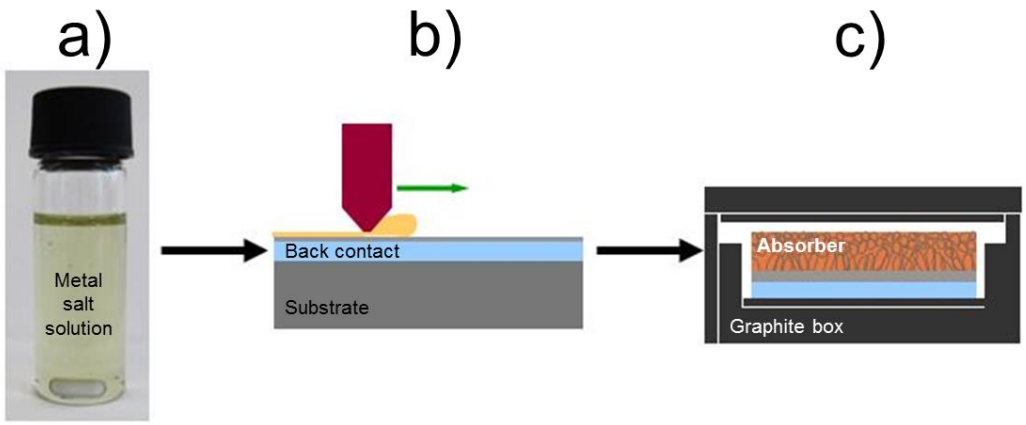

Figure S3: Schematic illustration of the solution process of preparing a SOL-$Cu_2ZnGe(S,Se)_4$ absorber: a) metal salt solution, b) doctor blade coating, c) annealing in Se atmosphere.

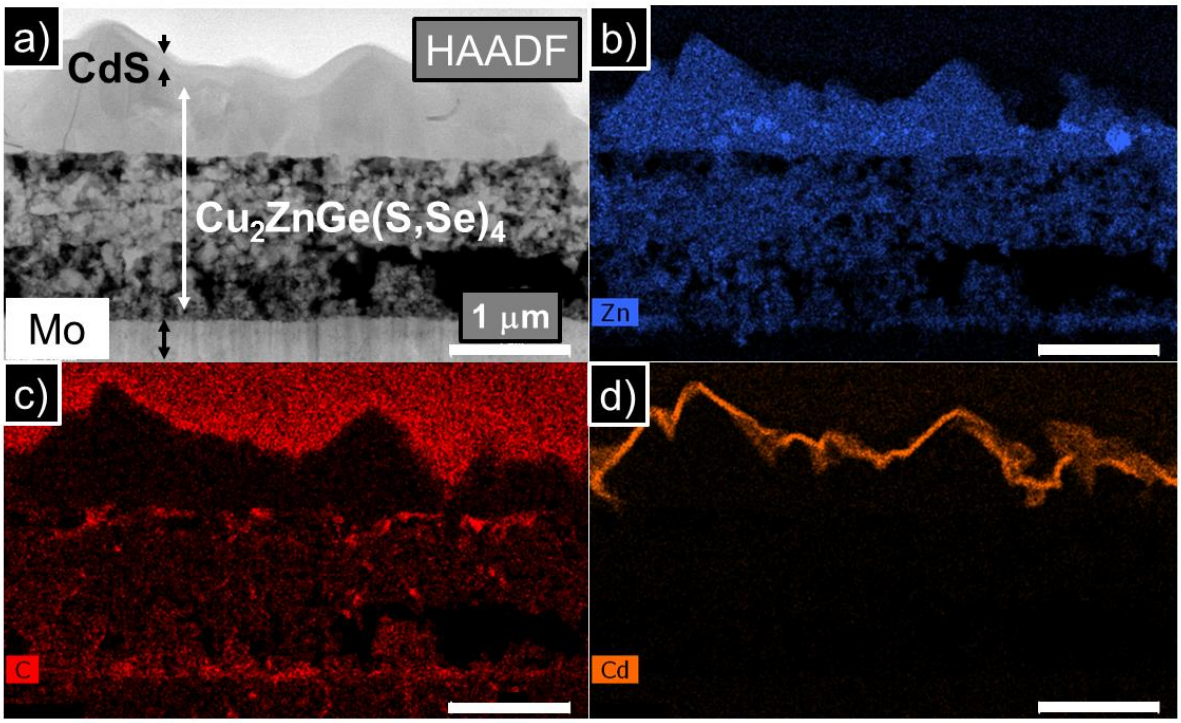

Figure S4: Cross-section high angle annular dark field (HAADF) STEM image of a SOL-$Cu_2ZnGe(S,Se)_4$-based solar cell with CdS buffer and ZnO window (a), and the elemental maps of Zn (b), C (c) and Cd (d).

Buffer layer	V_{OC} (mV)	FF (%)	J_{SC} (mA/cm^2)	E_G (eV)	Eff. (%)
CBD CdS[17]	617	54.1	18.0	1.47	6.0
CBD Zn(O,S)	512	51.2	17.7	1.51	4.6
rf-Zn($O_{0.6}S_{0.4}$) [17]	730	48.3	13.0	1.54	4.6
ALCVD In_2S_3[17]	469	48.2	14.9	1.49-1.54	3.4
Co-evap. $CdIn_2S_4$[17]	354	49.6	14.7	1.44	2.6

Table S1: Electrical parameters for the most efficient buffer/SOL-$Cu_2ZnGe(S,Se)_4$ solar cells.

Parameter	ZnO:Al	CdS	$Cu_2ZnGe(S,Se)_4$	$MoSe_2$[31]	MoO_3[32]
d (µm)	0.120	0.050	1-2	0.04-0.10	0.04
E_G (eV)	3.3	2.4	1.47-1.5	1.1	2.85
χ (eV)	4.4	4.2	4.54	4.14	2.6
μ_n ($cm^2/V.s$)	100	100	10	100	100
μ_P ($cm^2/V.s$)	25	25	2	25	20
N_d (cm^{-3})	10^{18}	$3x10^{17}$	-	-	-
N_A (cm^{-3})	-	-	$2x10^{15}$ / $10^{16(O)}$	10^{16}	10^{18}
R_s ($\Omega.cm^{-1}$)	4.7 / $0.5^{(O)}$				
R_{sh} ($\Omega.cm^{-1}$)	365 / $800^{(O)}$				

Table S2: Parameters used in the simulations at standard solar cell test conditions. $^{(O)}$ Optimized parameters.

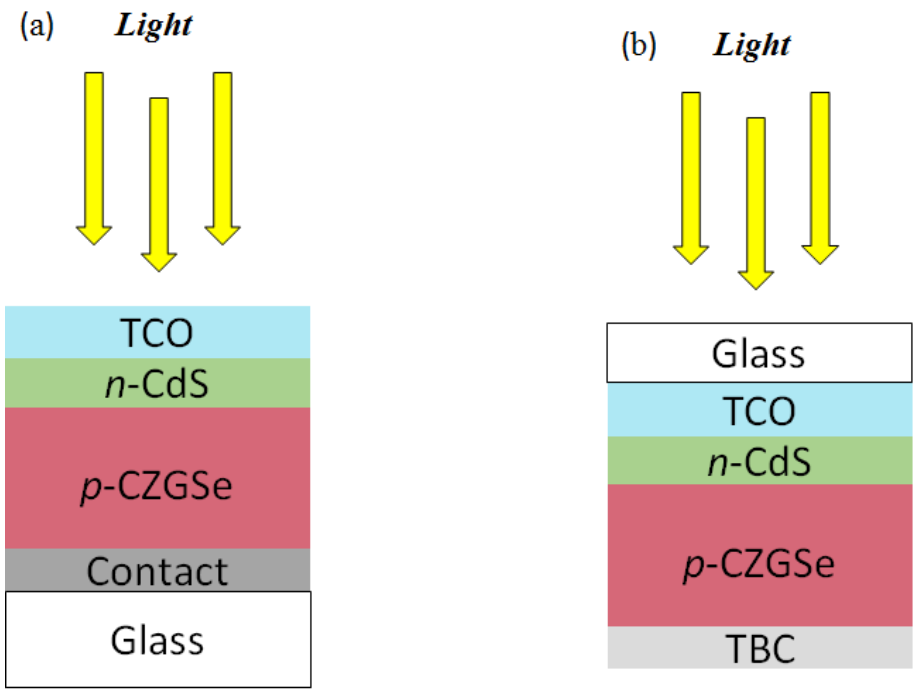

Figure S5: Schematic of the two different configurations considered in the device simulations: (a) substrate and (b) superstrate.

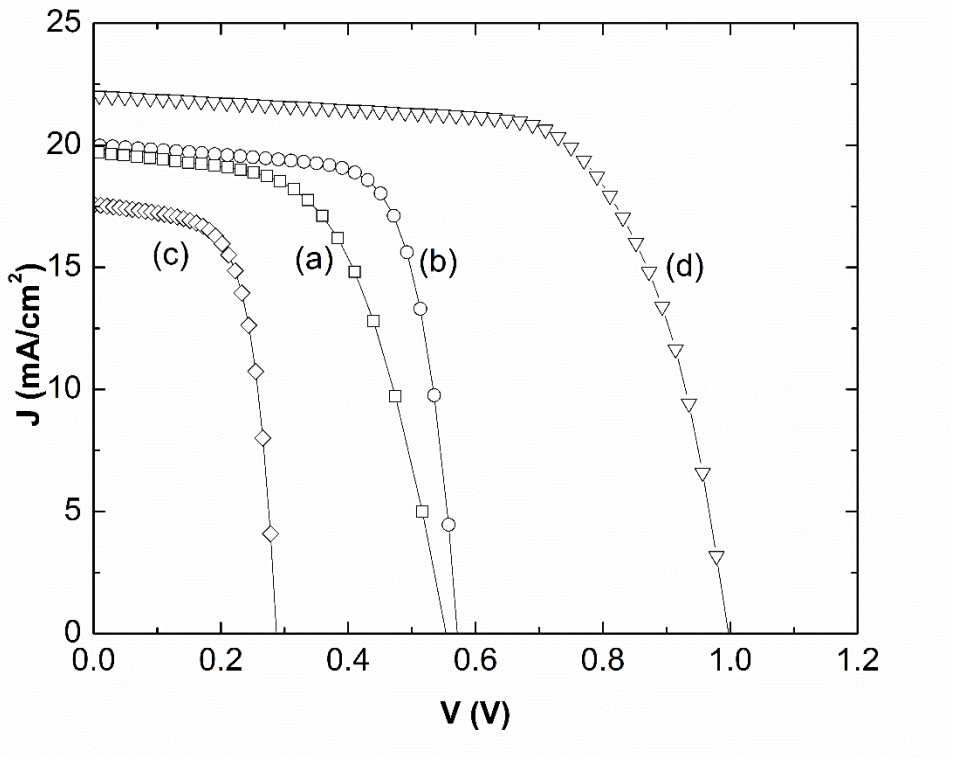

Figure S6: Calculated J(V) curves for different substrate/superstrate configurations: (a) substrate = $Cu_2ZnGe(S,Se)_4/MoSe_2/Mo/glass$, (b) same configuration as (a) but using optimized device simulation parameters (see Table S2), (c) superstrate = $Cu_2ZnGe(S,Se)_4/TCO$, and (d) superstrate = $Cu_2ZnGe(S,Se)_4/MoO_3/TCO$. For configurations (c) and (d) also optimized parameters were used in the device simulation.